Inorganic-Based Printed Thermoelectric Materials and Devices

Avishek Sarbajna, Andres Georg Rösch, Leonard Franke, Uli Lemmer, and Md Mofasser Mallick*

One of the simplest ways to generate electric power from waste heat is thermoelectric (TE) energy conversion. So far, most of the research on thermoelectrics has focused on inorganic bulk TE materials and their device applications. However, high production costs per power output and limited shape conformity hinder applications of state-of-the-art thermoelectric devices (TEDs). In recent years, printed thermoelectrics has emerged as an exciting pathway for their potential in the production of low-cost shape-conformable TEDs. Although several inorganic bulk TE materials with high performance are successfully developed, achieving high performance in inorganic-based printed TE materials is still a challenge. Nevertheless, significant progress has been made in printed thermoelectrics in recent years. In this review article, it is started with an introduction signifying the importance of printed thermoelectrics followed by a discussion of theoretical concepts of thermoelectricity, from fundamental transport phenomena to device efficiency. Afterward, the general process of inorganic TE ink formulation is summarized, and the current development of the inorganic and hybrid inks with the mention of their TE properties and their influencing factors is elaborated. In the end, TEDs with different architecture and geometries are highlighted by documenting their performance and fabrication techniques.

A. Sarbajna
Department of Physics
Technical University of Denmark
Anker Engelunds Vej 1 Bygning 101A, 2800 Kgs. Lyngby, Denmark

A. G. Rösch, L. Franke, U. Lemmer, M. M. Mallick
Light Technology Institute
Karlsruhe Institute of Technology
76131 Karlsruhe, Germany
E-mail: mofasser.mallick@kit.edu

U. Lemmer
Institute of Microstructure Technology
Karlsruhe Institute of Technology
76344 Eggenstein-Leopoldshafen, Germany

The ORCID identification number(s) for the author(s) of this article can be found under https://doi.org/10.1002/adem.202200980.

1. Introduction

Globally, $\approx 66\%$ of total used energy is wasted in the form of heat energy.[1] Due to the growth of the global energy demand and limited access to cost-effective renewable energy, the conversion of waste heat energy into electricity would be a significant benefit. While advanced heat engines such as machines based on the organic ranking cycle (ORC) offer a conversion method, the applications are limited due to the high costs and complexity of the systems. Harvesting energy from heat via the TE effect is possibly one of the simplest solutions to that task. Most solid-state materials exhibit a TE effect. However, only a few of them can convert heat into electricity effectively. Despite several challenges, efforts were put forward to employ TE generators (TEGs) for waste heat recovery.[2–4] They perform without any moving components and do not produce any chemical waste; hence, they require minimum maintenance. Apart from waste heat recovery applications, thermoelectric devices (TEDs) can be employed in different applications, including controlling temperatures of integrated circuits, wearable devices, neurological implantable devices, other medical applications, and heat flux sensing.[5–8] They also can utilize low-grade heat into electricity for powering the Internet of Things (IoT) devices. In **Figure 1**, we show a schematic illustration of printed TE material fabrication and their fields of applications.[9]

The performance of a TE material is determined by its figure-of-merit $ZT = \alpha^2 \sigma / \kappa$, where the α is the Seebeck coefficient which is positive for p-type and negative for n-type materials, σ is the electrical conductivity, and κ is the thermal conductivity.[10,11] Therefore, to realize an efficient material, α and σ should be maximized, and κ should be minimized. Though many inorganic bulk TE materials are found to exhibit adequately good performance,[12,13] high production costs, complex manufacturing processes, and lack of shape-conformity limit their applications. Printing technologies can be adopted to tackle the challenges associated with bulk TE materials. They offer efficient ways to produce low-cost shape-conformable TEGs by overcoming problems like low spatial resolution, surface roughness, and nonflexibility. Therefore, developing printable high-performance TE materials has become a notable area of interest in recent
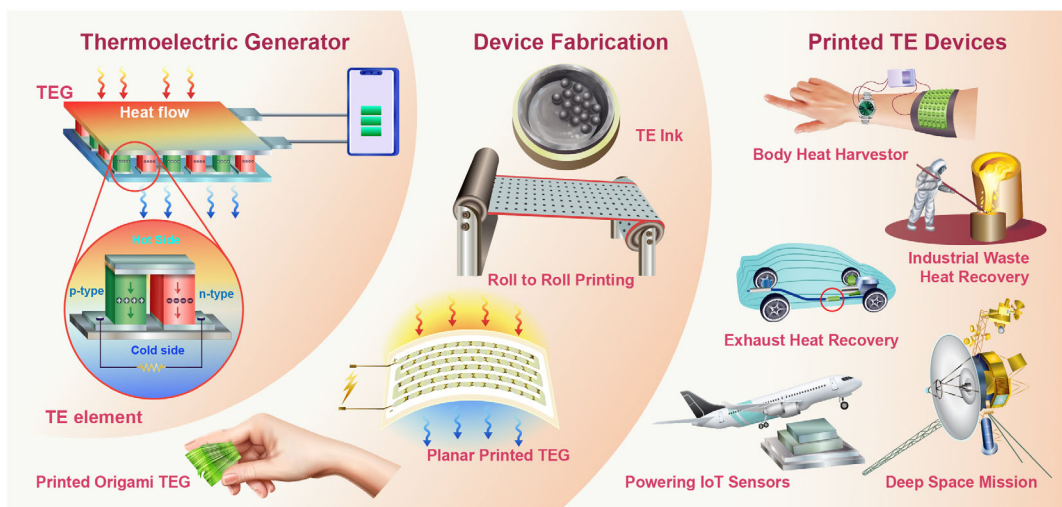
Figure 1. Schematic illustration of the printed TE materials processing, device fabrication, and the application of the TEDs.

times.[14,15] Furthermore, different printing techniques such as inkjet printing,[16–27] screen printing,[28–35] aerosol jet printing,[36–39] dispenser printing,[40–42] and roll-to-roll printing[43–50] were exploited in developing flexible TE devices in the last decade.

Organic TE materials, mainly conducting polymer-based materials, usually have a good printability, but they have a low TE performance due to a low α that limits their applications. The maximum ZT value at room temperature was reported for p-type DMSO-mixed PEDOT:PSS at 0.42.[51] However, the result was neither reproduced nor improved in other reports. The n-type 1,1,2,2-ethenetetrathiolate (ett)–metal coordination polymers poly[A$_x$(M–ett)] (A = K, Na; M = Ni, Cu) were also targeted to enhance their TE performance through different approaches.[22,52] Compared to bulk inorganic TE materials, the TE performance of their organic counterparts is still inferior.[53] As a possible trade-off, several printable inorganic materials based on TE particles were reported with higher ZT values than organic materials, but still lower than those of their bulk counterparts, mainly due to lower σ. The additives, binders, and solvents that are used to prepare TE inks and the leftover ingredients in the printed and sintered films resulted in a high interfacial resistance across the TE particles. Different approaches are being taken to minimize this interfacial resistance.[54] Well-established inorganic bulk TE materials like Bi$_2$Te$_3$, Sb$_2$Te$_3$, or Cu$_2$Se[55] have shown good printability,[15,56] shifting the challenge to increasing the TE performance of the printed films. The performance of conventional TE materials depends on transport parameters that are correlated to each other.[57] For example, reducing the grain size increases the scattering of phonons which in turn reduces thermal conductivity. At the same time, the electrical resistivity is enhanced by charge carrier scattering. However, the major challenge in printed thermoelectrics is to preserve the high TE performance by reducing interfacial resistance of the grain boundaries in the printed films. Therefore, it is very important to find suitable synthesis processes to achieve a high ZT value.

The focus of this review is to have an overview of the research that was carried out on printable inorganic and hybrid TE materials and devices. Starting with a brief theoretical discussion of thermoelectricity, we take a quick look at different methods of TE ink preparation and different printing techniques. Then after an elaborate discussion on inorganic and hybrid TE inks and their electrical properties, we conclude with a brief overview of the TEDs with different geometries and their reported performances to date.

2. Theory

In 1821, T. J. Seebeck first discovered thermoelectricity. He found that if junctions of two dissimilar metals are maintained at two different temperatures, electric current flows continuously in a closed circuit and the voltage between the junctions is proportional to the temperature difference.[58] The effect was subsequently called the Seebeck effect or TE effect. The voltage $V_{th} = \alpha \cdot \Delta T$ developing across a TE material is proportional to the temperature difference ΔT with the Seebeck coefficient α as the proportionality constant.[59] Thermoelectricity emerges from the difference in the Fermi distribution function f between the two ends at the hot and the cold side. The Fermi distribution of charge carriers at a particular position in a material with the Fermi level ε_F at temperature T is given by

$$f(\varepsilon) = \frac{1}{1 + e^{\frac{(\varepsilon - \varepsilon_F)}{k_B T}}} \tag{1}$$

where ε and k_B are the energy of the charge carrier and Boltzmann constant, respectively. Based on derivations from the generalized Boltzmann equations,[60–62] we can express the Seebeck coefficient α and the electrical conductivity σ and the electronic thermal conductivity κ_e as

$$\alpha = \frac{k_B}{\sigma e} \int \left(\frac{\varepsilon - \varepsilon_F}{k_B T} \right) \sigma_E(\varepsilon) \left(-\frac{\partial f}{\partial \varepsilon} \right) d\varepsilon \tag{2}$$

$$\sigma = \int \sigma_E(\varepsilon)\left(-\frac{\partial f}{\partial \varepsilon}\right) d\varepsilon \tag{3}$$

and,

$$\kappa_e = \frac{k_B^2}{e^2} \cdot T \int \sigma_E(\varepsilon)\left(\frac{\varepsilon - \varepsilon_F}{k_B T}\right)^2 \left(-\frac{\partial f}{\partial \varepsilon}\right) d\varepsilon \tag{4}$$

Here e is the charge of an electron, and $\sigma_E(\varepsilon)$ is the transport function of the material. It describes the contribution of the charge carriers at the energy level ε to the overall σ. In a crystalline bulk material, we can write the transport function as a function of electronic properties such as the density of states $D(\varepsilon)$, the charge carrier velocity $v(\varepsilon)$, and the relaxation time $\tau(\varepsilon)$[63]

$$\sigma_E(\varepsilon) = (1/3) \cdot e^2 \cdot v^2(\varepsilon) \cdot D(\varepsilon) \cdot \tau(\varepsilon) \tag{5}$$

To obtain the total thermal conductivity $\kappa = \kappa_L + \kappa_e$, we finally need to add the lattice thermal conductivity κ_L to κ_e.

With the obtained TE parameters, we can calculate the TE performance of a TED consisting of N p-type and N n-type TE legs with $\alpha_p, \sigma_p, \kappa_p$ and $\alpha_n, \sigma_n, \kappa_n$, respectively. The TE legs have the lengths d_p and d_n and the cross-section areas A_p and A_n, respectively. They are connected electrically in series and thermally in parallel, which results in the total electrical resistance

$$R = N \cdot (R_p + R_n) = N \cdot \left(\frac{1}{\sigma_p} \cdot \frac{d_p}{A_p} + \frac{1}{\sigma_n} \cdot \frac{d_n}{A_n}\right) \tag{6}$$

and the total thermal conductance

$$K = N \cdot (K_p + K_n) = N \cdot \left(\kappa_p \cdot \frac{A_p}{d_p} + \kappa_n \cdot \frac{A_p}{d_p}\right). \tag{7}$$

We can attribute an effective ZT value to the device[64]

$$ZT = \frac{(\alpha_p - \alpha_n)^2}{KR} T_m \tag{8}$$

where T_m is the mean temperature in the device. Note that the effective ZT value no longer purely depends on the material parameters but also on the geometric dimensions of the legs. The device reaches the maximum effective ZT when the condition[64]

$$\frac{d_p A_n}{d_n A_p} = \sqrt{\frac{\sigma_n \kappa_n}{\sigma_p \kappa_p}} \tag{9}$$

is fulfilled.

We can express the maximum TE efficiency η_{max} of such a device as

$$\eta_{max} = \left(\frac{T_H - T_C}{T_H}\right)\left(\frac{\sqrt{1 + ZT} - 1}{\sqrt{1 + ZT} + \frac{T_C}{T_H}}\right) \tag{10}$$

where T_H is the temperature of the hot side and T_C is the temperature of the cold side of the generator.[64]

If put in a realistic application to use a TED as a generator for electric energy, the heat source with the temperature T_{source} and the heat sink with the temperature T_{sink} have themselves the thermal conductance K_{source} and K_{sink}, respectively, which are connected in series to the TEG. Furthermore, the electrical load connected to the contacts of the TEG has an electrical resistance of R_{el}. Conventionally, we define the ratio $m = R_{el}/R$. Calculating T_H and T_C in this setting is not trivial due to TE effects and joule heating dissipation. Yazawa et al. published a comprehensive analytical method to calculate these two temperatures; however, the proposed system of equations requires numerical solving due to its complexity.[65] On the electrical side of the TEG, we can then express the open-circuit voltage of the device as a function of the effective temperature difference $\Delta T_{TEG} = T_H - T_C$[66]

$$V_{oc} = N(\alpha_p - \alpha_n)\Delta T_{TEG} \tag{11}$$

the output voltage at the load to[66]

$$V_{out} = V_{oc} \cdot \frac{R_{el}}{R + R_{el}} = V_{oc} \cdot \frac{m}{1 + m} \tag{12}$$

and the electric current through the device to[66]

$$I = \frac{V_{oc}}{R + R_{el}} = \frac{V_{oc}}{R(1 + m)} \tag{13}$$

On the thermal side of the TEG, we can express the incoming heat flow as[66]

$$\dot{Q}_{in} = N(\alpha_p - \alpha_n)T_H I - \frac{1}{2}RI^2 + K\Delta T_{TEG} \tag{14}$$

and the outgoing heat flow as[66]

$$\dot{Q}_{out} = N(\alpha_p - \alpha_n)T_C I + \frac{1}{2}RI^2 + K\Delta T_{TEG} \tag{15}$$

Finally, we can calculate the output power[66]

$$P_{el} = \dot{Q}_{in} - \dot{Q}_{out} = N(\alpha_p - \alpha_n)\Delta T_{TEG} I - RI^2 = \frac{V_{oc}^2}{R} \cdot \frac{m}{(m + 1)^2} \tag{16}$$

and the power conversion efficiency[66]

$$\eta = \frac{P_{el}}{\dot{Q}_{in}} = \frac{\Delta T_{TEG}}{T_H} \frac{m}{m + 1 - \frac{\Delta T_{TEG}}{2T_H} + \frac{(m+1)^2}{ZT T_H}} \tag{17}$$

When the external load and the internal resistance have identical values ($m = 1$), the output power is maximized to

$$P_{max} = \frac{V_{oc}^2}{4R} \tag{18}$$

while the maximum power conversion efficiency η_{max} from Equation (10) is reached in Equation (17) for $m = \sqrt{1 + ZT}$.[66] We can calculate the output power density $E = P_{el}/A$ by normalizing the output power to the cross-section area.[66]

ADVANCED
SCIENCE NEWS
www.advancedsciencenews.com

ADVANCED
ENGINEERING
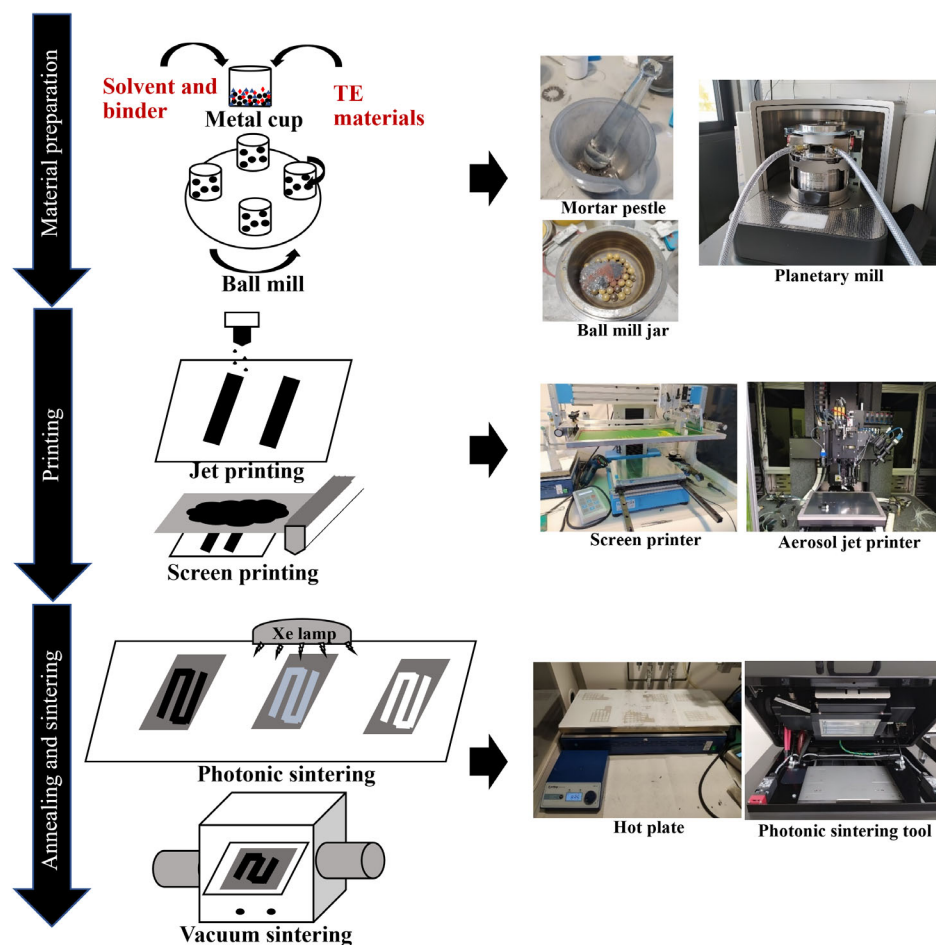**MATERIALS**
www.aem-journal.com

Figure 2. Step-by-step illustration of the fabrication process of flexible TE films and the equipment used for the purpose, starting from the ink preparation.

3. Fabrication of Printed TE Materials and Devices

The steps associated with the preparation of printed inorganic TE materials are as follows: Preparation of TE inks, the printing of the prepared ink, and post-printing treatments such as sintering and pressing (**Figure 2**). Inorganic TE inks consist of three major ingredients: TE particles, a binder to control the viscosity, and a solvent. Preparation of TE particles typically starts with bulk ingots and subsequent grinding. This can be one using mortar and pestle. A more replicable approach is to use controlled ball milling. For this process, the required milling time depends on the size of the balls, rotational speed, and the desired size of the TE particles in the ink. In general, to avoid oxidation during ball milling, inert gases like argon are purged in the cups. The preparation of a printable inorganic-based TE ink by mixing TE particles, an organic binder, and solvent preferentially require only a one-step process. The mixing step can involve ball milling, ultrasonically mixing, or similar processes. The prepared ink can then be printed by screen printing, doctor blading, dispenser printing, inkjet printing, or other printing methods, including 3D printing. Different printing methods require different properties of the TE ink, such as viscosity, particle size, and types of solvent and binder. Inkjet printing, for example, requires a comparatively finer particle size compared to screen printing. The next

processes are drying, annealing/sintering that expels the solvent, and sometimes organic binder from the printed TE films. Sintering occurs preferably in an inert or reducing atmosphere to avoid the oxidation of the printed TE material. Vacuum ovens are widely used for this purpose. Photonic and laser sintering has become attractive in recent years due to the more precisely controlled and fast process. One strategy to improve the film quality is a post-printing pressure treatment to enhance the adhesion of the TE films and compact the printed films. This general outline comes with a few difficulties which cause a decrement in the performance of the device. One of the most encountered problems is the high sintering temperature. Conventionally used TE materials like Bi_2Te_3 or Sb_2Te_3[67] lose σ as tellurium starts to evaporate at high temperatures. Another factor that should be taken into account is the porosity which enhances surface oxidation of the ink and therefore reduces the performance of the printed material. Decreasing the surface roughness and increasing the density of printed films help to prevent oxidation. It should be noted that samples sintered in a reducing Ar/H_2 atmosphere come up with a porous surface revealing that Ar/H_2 sintering restrains the grains from recrystallizing, hence reducing the σ.[68] Results reveal that the Te content after sintering highly depends on the atmosphere as more Te is found in the samples sintered in an N_2 environment than if sintered in

**ADVANCED
SCIENCE NEWS**

www.advancedsciencenews.com

**ADVANCED
ENGINEERING
MATERIALS**

www.aem-journal.com

Ar/H_2. The advantage of photonic over vacuum oven sintering is that it takes very little time to sinter, typically in the order of microseconds, thus diminishing the potential oxidation of the sample. The chemical treatment of the Bi_2Te_3 sample with HCl reduces the Bi_2O_3 present on the surface of the microparticles.[69] The chemical treatment with HCl reduces Bi_2O_3 present on the surface of the microparticle. Oxidation of Bi_2Te_3 can also be minimized by using ethylene glycol as it acts like a capping agent[70] Though it was also noticed that chemical treatment results in a decrement in α, it is overcompensated by the improvement of σ. In some cases, TE materials are directly added to the solution containing the binder and the solvent and are stirred long enough to get a printable ink.[71] For example, tungsten carbide is added to a solution of chloroform and PLA and then filled into syringes. After stirring for several hours to prepare the ink is suited for being used in a 3D printer.[72] The ratio between the TE materials and the used binder also plays a role in the TE properties. The optimum ratio to get the maximum output power from the TED is typically determined empirically.

4. Pure Inorganic-Based Printed TE Materials

Although several inorganic-based bulk TE materials with ZT > 1 have been successfully developed, the chalcogenides such as bismuth telluride and antimony telluride are widely targeted for printed thermoelectrics because of their high performance near room temperature (RT). Different approaches have been put forward to overcome the challenges associated with printing thermoelectrics on flexible substrates, such as low σ and poor flexibility of the TE film. Chen et al. fabricated TE films using a dispenser printing technique and could achieve ZT up to 0.31 for n-type Bi_2Te_3 and 0.41 for p-type Sb_2Te_3-based materials in various contributions. One of the advantages of dispenser printing is the ability to fabricate TE films with a wide range of dimensions.[40] In one of their initial attempts, they used 5 wt% toluene as a solvent with the TE particles and an epoxy resin system, a well-known polymer adhesive, as a binder.[73] According to their results, the films made of ink with 80 wt% of TE particles exhibited the best performance. The PF values for n-type Bi_2Te_3–epoxy and p-type Sb_2Te_3-epoxy composite films were 150 and 840 $\mu Wm^{-1}\,K^{-2}$, while the ZT values were 0.16 and 0.41, respectively at RT. They varied the curing time from 6–48 h and used a curing temperature in the range of 423–623 K (**Figure 3**a,b). The trend of changing α with the curing temperature was different for n- and p-type materials. For p-type Sb_2Te_3 TE composite films, α did not change significantly with curing temperature, whereas σ increased due to a larger hole carrier concentration resulting from fewer defects. Also, the larger grain size reduced grain boundary scattering thereby further increasing σ.[74] The absolute α for n-type Bi_2Te_3 increased with
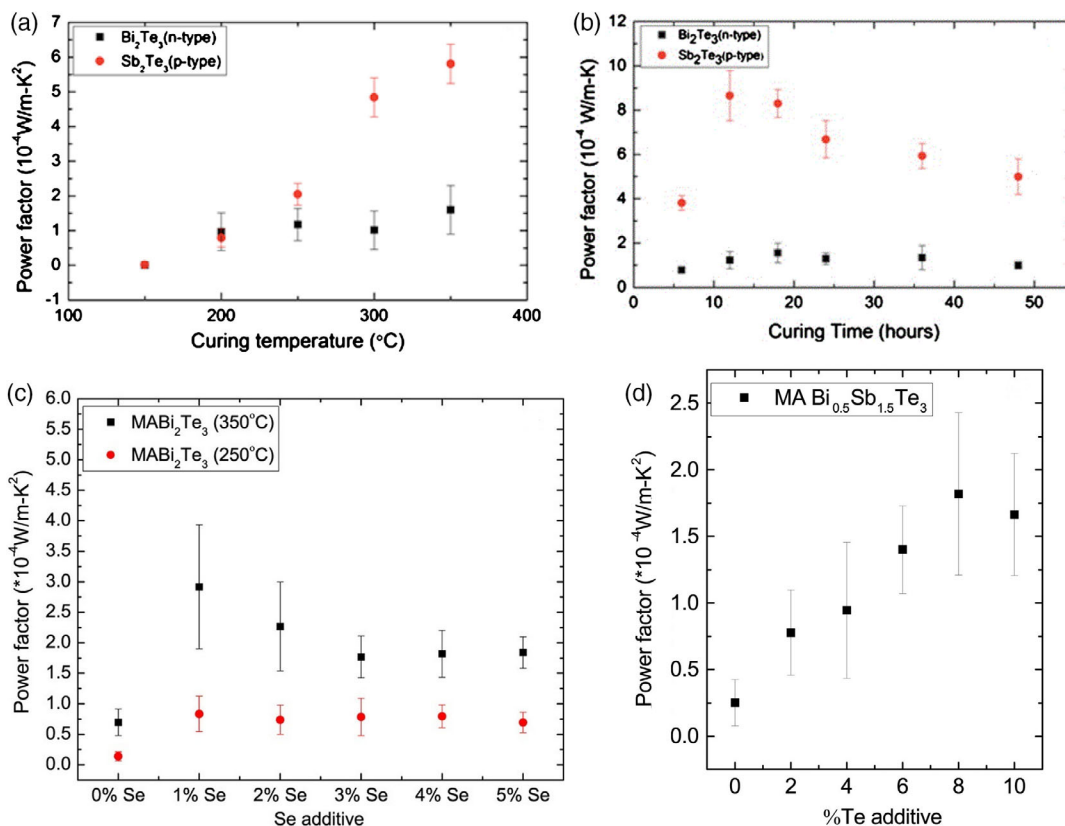

Figure 3. a) and b) the dependence of PF of dispenser printed TE thick films of Bi_2Te_3 and Sb_2Te_3 on curing temperature and curing time is shown[73] (reproduced with permission, copyright 2011, API publishing). In c), the dependence of the PF of MA Bi_2Te_3 cured at different temperatures on Se additive is shown[76] (reproduced with permission, copyright 2012, ACS publication). d) shows the change of PF for dispenser printed MA $Bi_{0.5}Sb_{1.5}Te_3$ composite films with different wt% of Te additive[86] (reproduced with permission, copyright 2013, ACS publication).

**ADVANCED
SCIENCE NEWS**

www.advancedsciencenews.com

**ADVANCED
ENGINEERING
MATERIALS**

www.aem-journal.com

increasing curing temperature.[75] σ of n-type Bi_2Te_3 showed very little change with the increased curing time. No significant enhancement in the PF was found. Evans et al. also demonstrated a ZT of 0.19 and 0.18, respectively, at RT for p-type Sb_2Te_3 and n-type Bi_2Te_3 dispenser printed materials.[40] The printing was done on a polyimide substrate and the material was cured at 523 K in an argon or vacuum oven for a minimum of 3 h. The weight proportion of the TE powders to the epoxy resin was again 80:20. The ball-milled $Bi2Te3Bi2Te3$ powder was then added to the epoxy resin system to make printable slurries. 5 wt% toluene was used as a solvent to mix the epoxy resin system together with active filler particles. The choice of toluene as a solvent was due to its low boiling point and low viscosity. Empirical testing has shown that 80 wt% of filler particles provide the best film properties. In both cases, the PF decreased with the rising temperature suggesting that the materials perform best when used at RT. In the following year, they achieved a ZT value of 0.31 for mechanically alloyed (MA) n-type Bi_2Te_3-epoxy composite films with 1 wt% of Se using the dispenser printing technique.[76] The film was cured at 623 K for 12 h. The addition of Se resulted in modifying σ due to the larger grain boundaries and lowered the melting point of the material. Melting occurred at 698 K instead of 853 K, which is the melting point of the pristine Bi_2Te_3 alloy, which in turn helped to form larger grains at a lower curing temperature. The results revealed that the conductivity did not improve with an increase in Se beyond 1 wt% due to the increased bandgap of MA Bi_2Te_3 with proportion to the percentage of Se.[77] Also, the sample cured at 523 K has a much lower conductivity than the sample cured at 623 K. σ could be increased to 14 000 S m^{-1} for the sample with 1% Se and cured at 623 K, though it is still almost one order of magnitude lower than the conductivity of bulk Bi_2Te_3. In general, α has an inverse relationship with the carrier concentration for a single-phase system,[78] but for a two-phase composite system, a more complicated behavior is observed[79–82] and can be explained by effective-medium-theory. In this case, α was lower for the Se-free MA Bi_2Te_3 composite film than for the sample containing additive Se, the values were 170 and 200 μV K^{-1}, respectively. This is the result of the reduction of the carrier concentration due to the addition of Se.[83] The α of the printed film cured at 523 K was slightly higher than that for the film cured at 623 K. For the sample cured at 523 K for 12 h, donor-type defects that appear during the mechanical alloying process supply excess n-type carriers, so the carrier concentration decreases due to the increased annealing time.[75] For the sample cured at 623 K for the same amount of time, the carrier concentration did not decrease much as Te evaporates at 623 K and forms Te vacancies. The formation of bismuth oxides also produces new defects, which altogether increase hole carrier concentration resulting in compensation of donor-like defects.[84,85] As a result, they achieved a PF of 470 μW m^{-1} K^{-2} for the sample with 1% Se cured at 623 K, the highest among all the samples (Figure 3c). Here also the insulating nature of epoxy and fine grains of active filler particles caused a good reduction of κ to 0.26, and 0.38 W m^{-1} K^{-1}, respectively, for the samples cured at 523 and 623 K and with 1% Se whereas the typical value for bulk material is around 1.2 W m^{-1} K^{-1}.[73] Madan et al. achieved a comparatively lower ZT of 0.2 at RT when they used 8% tellurium as an additive.[86] Here, mechanically alloyed (MA) p-type

$Bi_{0.5}Sb_{1.5}Te_3$-epoxy composite was used followed by curing at 523 K for 12 h. As discussed earlier, a long curing time reduces the defects leading to a lower carrier concentration. This provides an increased α.[73,86] The addition of Te helped to increase α by 50% compared to the sample without additives. The increase in α results from the reduction of the Antisite defect concentration because the extra Te filled the Te deficiency sites.[87] The sample with 8% Te additive achieved the highest α at around 280 μV K^{-1}, leading to a maximum PF of 180 μW m^{-1} K^{-2} (Figure 3d). Moreover, they used a wet grinding method to reduce the particle size to less than 5 μm.

The nonconducting epoxy polymer matrix reduced the σ of the printed films by around two orders of magnitude to 1.2×10^3 S m^{-1} compared to 13×10^4 S m^{-1} of bulk $Bi_{0.5}Sb_{1.5}Te_3$.[88] Another reason for the reduction of the conductivity might be the smaller grain size that increases the scattering at the grain boundaries and thus decreases carrier mobility.[76] The low thermal conductivity and the insulating nature of the epoxy lead to a lower κ (0.24 W m^{-1} K^{-1}) of the printed film than the bulk material (1.1 W m^{-1} K^{-1}). In 2015, Madan et al. published their results related to flexible TEDs for the use of low-grade waste heat with a dispenser printed TEG.[42] There, they used previously developed Te-doped MA $Bi_{0.5}Sb_{1.5}Te_3$ as p-type and Se-doped MA Bi_2Te_3 as n-type material.[76,86] They measured the TE properties in the temperature range of 293–363 K after curing at 523 K. σ was in the same range for both inks at around 2400 S m^{-1} for the n-type and around 2200 S m^{-1} for the p-type material at RT. However, the magnitude of α for the p-type ink was higher than for the n-type ink, amounting to around 280 and approx. 195 μV K^{-1}, respectively. As a whole, the listed PFs at RT were 160 μW m^{-1} K^{-2} for the p-type and 100 μW m^{-1} K^{-2} for the n-type ink, respectively. Apart from these findings, Madan et al. came up with more results with the dispenser printing method. They recorded a ZT of 0.17 at 300 K for MA n-type Bi_2Te_3 epoxy composites with 2 wt% Se additive[89] and the highest PF of 80 μW m^{-1} K^{-2} over a temperature range of 293 to 363 K for Bi-epoxy and $Bi_{0.5}Sb_{1.5}Te_3$ with 8 wt% extra Te-epoxy composite.[41] We et al. reported their results in 2013, when they used a screen-printing technique to print Bi_2Te_3 paste on a SiO_2/Si wafer and an alumina substrate.[30] The ZT value of 0.61 at RT is comparable to the ZT value of the bulk Bi_2Te_3 material.[90,91] To prepare the paste, they mixed 2.4% glass powder and 2.3% binder in weight compositions with 75% of Bi and Te powders (mixed 35:65 in atomic percentage). They then added 20.3 wt% solvent. They prepared the paste by ball milling the mixture for 24 h and heated it to 393 K for 15 min after the printing. Then annealing was done in three steps. Heating for 5 min at 473 K to remove the binder, followed by the solidification process at 673 K for 30 min in an N_2 environment. Finally, further heating the printed material to higher temperatures to achieve the most promising TE properties. The temperature range between 723 and 823 K produced the best output with σ reaching its maximum value of 2.6×10^4 S m^{-1} and α also steadily increased with the increasing temperature producing the optimum PF of 480 μW m^{-1} K^{-2}. However, at such a high temperature, Te starts evaporating, causing degradation of σ, which counteracts the PF rise. This can be avoided by adding Bi and Te powders during the annealing process. This change of TE properties highly depends on the

**ADVANCED
SCIENCE NEWS**

www.advancedsciencenews.com

**ADVANCED
ENGINEERING
MATERIALS**

www.aem-journal.com

dwelling time of the annealing process. In the presence of powders, the decrease of the ZT value with dwelling time is due to the increased κ, which is partly compensated by the improved power factor. They achieved a PF of 2100 μW m^{-1} K^{-2} and a κ of 1.0 W m^{-1} K^{-1} with annealing the printed Bi$_2$Te$_3$ at 773 K for 15 min in the presence of Bi and Te powders.

Recently, Mallick et al. used a sulfur-doped Cu$_2$Se TE ink to print ultraflexible TEDs.[55] They observed that α increases from around 20 to 40 μV K^{-1} when Cu$_2$Se is doped as the S atom replaces the isoelectronic Se. The metallic behavior of Cu$_2$Se changes to semi-conducting behavior after the S doping. This transition is due to the opening of a bandgap, which leads to an enhanced α. The transition from a metal to a doped semiconductor, however, also reduces σ. As S doping leads to alloy scattering of phonons, κ is also reduced after doping. This helps to improve the TE properties. They also find that the ball milling time impacts α. Longer ball milling leads to a change of phase from β-Cu$_2$Se to α-Cu$_2$Se and thus reduces α.

σ shows the same trend and degrades with increasing ball-milling time. It should be noted that a minimum ball milling is required to form the β-Cu$_2$Se phase and during that time, the TE properties improve with the milling time. Here, they could observe optimum TE properties after 30 min of milling. The highest recorded PF and ZT were 280 μW m^{-1} K^{-2} and 0.21, respectively, at 375 K for Cu$_2$Se$_{0.9}$S$_{0.1}$ TE ink (**Figure 4**). With this approach, they printed ultraflexible and superfine layouts for TEDs with an average thickness below 10 μm (Figure 2d). Lu et al. reported on an inkjet printing method to fabricate the TE thin film[71] based on p-type Sb$_{1.5}$Bi$_{0.5}$Te$_3$ NPs and n-type Bi$_2$Te$_{2.7}$Se$_{0.3}$ NPs with a polymeric stabilizer. The printed samples were then annealed at 673 K for 30 min in an Ar gas environment. This decomposed the polymeric stabilizer in the samples, while the polyimide substrate material is capable of withstanding the temperature for half an hour. The lack of cracks or peeling proved a good adhesion between the TE material and the substrate. The electrical conductivity of films based on n-type Bi$_2$Te$_{2.7}$Se$_{0.3}$ NPs was about 6.0 $\times$ 10^3 S m^{-1}, three times higher than the films using p-type Sb$_{1.5}$Bi$_{0.5}$Te$_3$ NPs. The comparatively lower value of σ compared to the reported values of thin films prepared by other methods or the bulk materials might be due to the low density of the materials in the inkjet-printed thin films. The highest PF found for Sb$_{1.5}$Bi$_{0.5}$Te$_3$ was 77 μW m^{-1} K^{-2} and that for Sb$_{1.5}$Bi$_{0.5}$Te$_3$ NPs film was

183 μW m^{-1} K^{-2} at 348 K. A work of Varghese et al. reported highly performing and flexible TE films and devices made by screen printing.[28] They used a microwave-stimulated wet-chemical method to prepare Bi$_2$Te$_3$-based nanocrystal inks and achieved a ZT of 0.43 at 448 K for the n-type films, which was one of the highest reported values for Bi$_2$Te$_3$-based inks at the time. After printing, the films dried at 473 K followed by sintering at 723 K for 45 min. The thickness of a screen-printed film of these doped and functionalized pnictogen chalcogenide nanocrystals of Bi$_2$Te$_{2.8}$Se$_{0.2}$ (BTS) was 10 μm. It was compared with a reference pellet sample of 500 μm thickness made under the same conditions. The RT conductivity of the printed film was 53% lower than that of the pellet. The reason is an increased electron scattering by impurities, and the porosity of the printed films as the film's electron mobility was about 56% lower than the pellet's electron mobility (0.0127 versus 0.0290 m^{2}V^{-1}s^{-1}) in the Hall measurement. The Seebeck coefficients were within 10% of each other for both samples. The carrier concentrations for the film and the pellet were more or less the same at 1.56 $\times$ 10^{25} and 1.42 $\times$ 10^{25} m^{-3}, respectively. The thermal conductivity of the film, however, was reduced due to the nanoscale grains. The much lower κ of the film results from additional phonon defect scattering caused by the higher porosity and the addition of glass particles.[92] The lower κ compensated for the lower σ in the achieved ZT of 0.43 at 448 K for the film as it was 20% lower compared to the pellet (**Figure 5**a). To test the flexibility of the films, they used cylinders of 7 and 5 mm radius for bending. Using the van der Pauw method, they observed a rise in electrical resistance of 1.4% and 4.5% for 7 and 5 mm cylinders, respectively, after 150 bending cycles (Figure 5b). One of the main ingredients of the TE ink is the binder. In most cases, however, these binders have a detrimental effect on the conductivity of the ink. As a solution, Shin et al. used methylcellulose as a binder additive with p-type Bi$_{0.5}$Sb$_{1.5}$Te$_3$ and n-type Bi$_2$Te$_{2.7}$Se$_{0.3}$ which gave adequate viscosity for printability at a very small concentration of 0.45–0.60 wt%.[93] As a result, the detrimental impact of binders on electrical transport shranks to a minimum. The samples were printed, followed by conventional sintering and hot pressing. The results revealed that the left-over nanoscale defects due to this led to an increase in phonon scattering and hence reduced κ for the printed n-type material. Here, Bi$_{0.5}$Sb$_{1.5}$Te$_3$ and Bi$_2$Te$_{2.7}$Se$_{0.3}$ were used as p-type and n-type TE particles, respectively, and the screen printing was
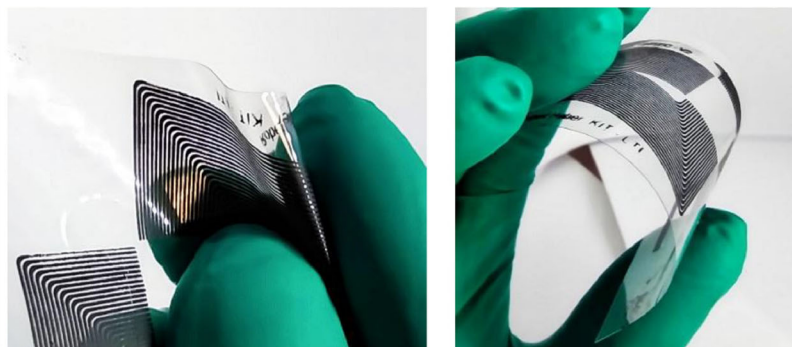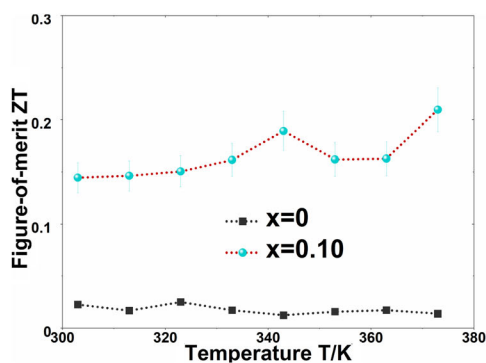

Figure 4. Comparison of ZT between Cu$_2$Se and Cu$_2$Se$_{0.9}$S$_{0.1}$ as a function of temperature and a demonstration of a screen-printed ultraflexible TE film[55] (reproduced with permission, copyright 2022, Elsevier).
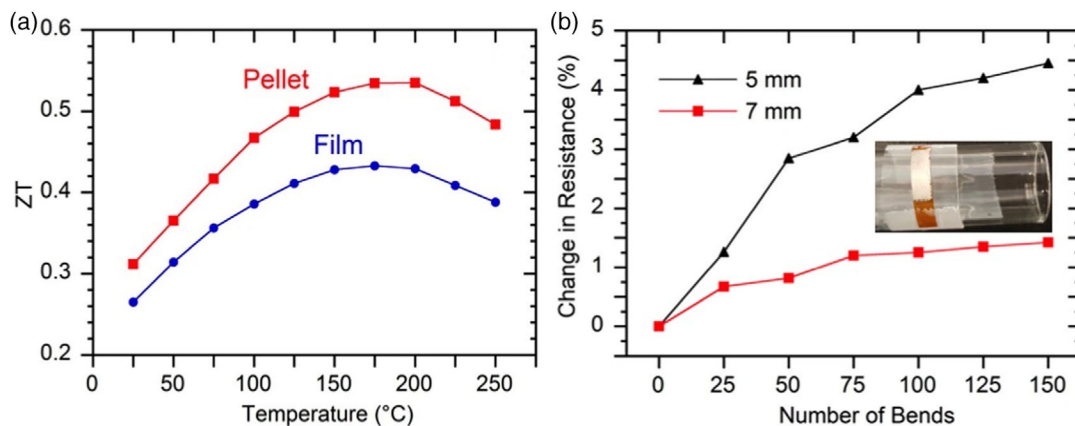
ADVANCED
SCIENCE NEWS
www.advancedsciencenews.com

ADVANCED
ENGINEERING
MATERIALS
www.aem-journal.com

Figure 5. a) Temperature-dependent ZT of screen printed $Bi_2Te_{2.8}Se_{0.2}$ films and the reference pellet, and b) the change in electrical resistance in the film as a function of bending cycles are shown[28] (reproduced with permission, copyright 2016, Springer, Nature).

done on flexible glass fabrics. The measured Seebeck coefficients were $209\,\mu V\,K^{-1}$ for the p-type and $-165\,\mu V\,K^{-1}$ for the n-type material. The Seebeck coefficient of the printed TE films matches with the corresponding TE powders. This is because Methocel is insulating and added only up to 0.6 wt% of the inks. That is why TE materials dominate the Seebeck coefficient of the TE ink compared to the binder. But the fabric roughness and the porosity of the substrate impacted the conductivity greatly. As per the report, σ varied from 850 to $1.9 \times 10^4\,S\,m^{-1}$ as the thickness of the printed layers increased from 9 to $111\,\mu m$. The authors then introduced an interface layer to reduce the effect of the roughness and the porosity. It is a nonconductive layer made of chitosan that helps to planarize the surface and blocks the pores in the substrate. It is a well-known binder that controls viscosity,[94,95] used in printing for the treatment of the fabric.[96,97] The chitosan interface layer reduced the surface roughness within in a limit of $50\,\mu m$ and largely improved σ. For the same TE film thickness of $\approx 110\,\mu m$, they could achieve an σ of $27\,800\,S\,m^{-1}$ after introducing chitosan compared to the $19\,000\,S\,m^{-1}$ of the sample on plain glass fabric. To reduce the thickness ratio between the fabric and the TE layer, they then increased the thickness of the TE layer up to $500\,\mu m$, confirming

the reduced adverse contribution from the fabric. For the thicker samples on chitosan, they measured electrical conductivities of 6.39×10^4 and $7.63 \times 10^4\,S\,m^{-1}$ for the p-type and the n-type samples. For κ, they measured $\kappa_{\parallel}$ with the Angstrom method[98] to be 1.29 and $0.77\,Wm^{-1}\,K^{-1}$ for p- and n-type BTS films consecutively. The thickness varied between 600 and $800\,\mu m$. Taking the anisotropy of κ into account, they also measured the cross-plane thermal conductivity $\kappa_{\perp}$ with the 3ω technique.[99,100] The values were 1.06 and $0.83\,W\,m^{-1}\,K^{-1}$ at 300 K for the p-type and n-type layers, respectively. From these values, the lattice thermal conductivity ($\kappa_L = \kappa - L\sigma T$) was 0.97 and $0.37\,W\,m^{-1}\,K^{-1}$ for p- and n-type materials considering the Lorenz numbers of 1.67×10^{-8} and $1.74 \times 10^{-8}\,V^2K^{-2}$ for p-type BST and n-type BTS films, respectively. In this process, they could achieve high ZT values of 0.68 and 0.81 for the p-type and n-type printed layers at RT by minimizing the use of the organic binder. Burning off the binder creates nanoscale defects resulting in phonon scattering for the n-type films.

Xu et al. reported that controlled Pb doping could modify the TE properties as it increases the bandgap.[101] 0 to 4 at% Pb was doped into $Bi_{0.7}Sb_{1.3}Te_3$ and a ZT ≈ 1.0 was achieved at a temperature range of 513–613 K for 1 at% Pb-doped sample

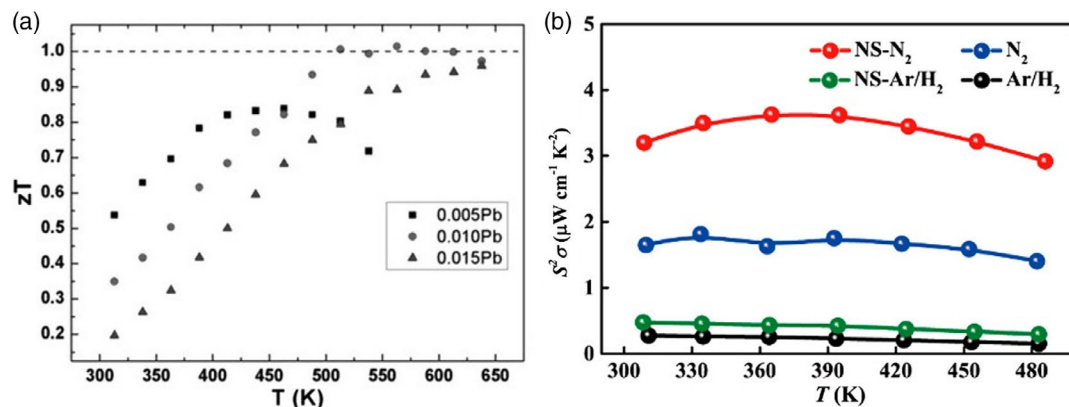**Figure 6.** a) The temperature-dependent ZT of a low-temperature solution-processed Pb-doped $Bi_{0.7}Sb_{1.3}Te_3$ with different doping levels[101] (reproduced with permission, copyright 2017, John Wiley and Sons). b) The temperature dependence of the PF of printed Bi_2Te_3 films prepared with different routes. NS represents added nano solders, and N_2 and Ar/H_2 are the sintering atmospheres[68] (reproduced with permission, copyright 2019, ACS publication).

(**Figure 6**a). They used a self-developed[102,103] low-temperature solution-phase synthesis process to prepare the nanostructures.

α for all the samples with different doping increased with increasing temperature in the low-temperature range and then decreased at elevated temperatures. This can be explained by the thermal excitation of minority carriers, that is, electrons. Also, for σ, the trend was the opposite. One of the less explored areas of improving the TE properties of bismuth telluride is to sinter it with a flash of UV light from a xenon lamp. In 2018, Danaei et al. produced convincing results by using a flash sintering method[104] (**Figure 7**). The problem with the conventional sintering process is the requirement of a high temperature of up to several hundred K with typical values of more than 600 K. Furthermore, a long heating time makes the use of polymeric substrates very difficult. Danaei et al. fabricated $Bi_2Te_{2.8}Se_{0.2}$ films via screen-printing ink based on NPs synthesized by a microwave-assisted reaction. Then, they exposed the dried and cold-pressed samples to the xenon lamp flash. The σ depends on the pulse duration and improved from a value of $10^{-3}\,S\,m^{-1}$ for the unsintered sample to a very high value of $3200\,S\,m^{-1}$ for an exposition time of 2 ms, the substrate used was glass. The RT conductivity for printed films on the Kapton tape was $1.9 \times 10^3\,S\,m^{-1}$, which is lower than that of the samples on the glass due to the limited optical power density that could be applied without damaging the sample. The power density was limited as cracks on the sample appeared due to the higher thermal expansion coefficient of Kapton compared to glass. With the change in the temperature, minor changes of σ occurred for both, the glass and the Kapton substrate samples. Although an appreciable increase in α happened for increasing temperature, it was the same for the samples printed on the glass and the Kapton substrates, around $90\,\mu V\,K^{-1}$ at 473 K.

They achieved the highest PF of $30\,\mu W\,m^{-1}\,K^{-2}$ at 473 K for the sample sintered with the highest energy. Mainly due to the lower σ, this PF was lower than the previously reported power factors for similar samples sintered conventionally. The photonic sintering method is useful for any printing method such as screen printing, inkjet printing, and aerosol jet printing. It allows for a wide range of substrates, flexible or rigid. Furthermore, researchers developed models for the photonic sintering process. Considering parameters like the particle size, which has a good impact on the melting point of the material,[105] the model demonstrated where the photonic sintering process selectively heats the NPs. Based on this densification model, they evaluated the temperature profile of the film.[106]

In recent times, Javash et al. also used photonic sintering and reported flexible TE films fabricated by an aerosol jet printing method, they used a $Bi_2Te_{2.7}Se_{0.3}$ ink.[107] They achieved a σ of $2.7 \times 10^4\,S\,m^{-1}$ which led to a PF of $730\,\mu W\,m^{-1}\,K^{-2}$ at RT. The quality of the flexible sintered films was impressive. In a bending experiment, the electrical resistance only increased less than 4% after 500 times of bending. The TE properties of the materials depended on the number of pulses applied during the photonic sintering process (**Figure 8**). Oversintering causes degradation of the TE properties, specially of σ. They also demonstrated that TE properties could be modified by interface engineering. They showed that the assistance of nanosolder or electronic glue helps the sintering process and enables high conductivities. In one of their experiments, they used ball-milled $Bi_{0.4}Sb_{1.6}Te_3$ NPs (BST) with a nanosolder-assisted sintering process[108] (**Figure 9**). They added tellurium particles to act as a bridge among the interfaces of the NPs (BST:T). It leads to significant improvement of carrier mobility in the film. This super flexible printed film showed a ZT of around 1 and a PF of around $3000\,\mu W\,m^{-1}\,K^{-2}$ at RT, which is an impressive value for a printed film. They measured and compared the temperature-dependent TE properties of the $Bi_{0.4}Sb_{1.6}Te_3$ sample and the sample of $Bi_{0.4}Sb_{1.6}Te_3$ with 8% tellurium particles. Due to the semi-metallic nature of the samples, the σ decreases with the increase of temperature, though at RT the σ of the BST:T is 42% higher than in the BST sample. This is due to the improved interfacial connections among the BST surfaces and the increased carrier concentration. Hall measurement revealed an increase in carrier concentration from 2.4×10^{19} to $3.1 \times 10^{19}\,cm^{-3}$

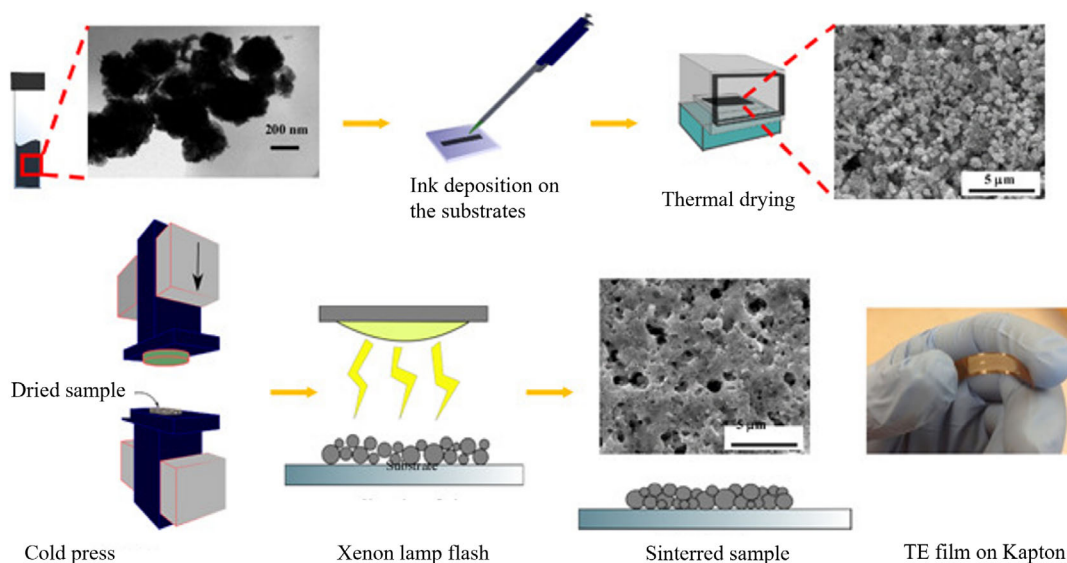**Figure 7.** Schematic representation of the pulsed light sintering process[104] (reproduced with permission, copyright 2018, John Wiley and Sons).

ADVANCED
SCIENCE NEWS
www.advancedsciencenews.com

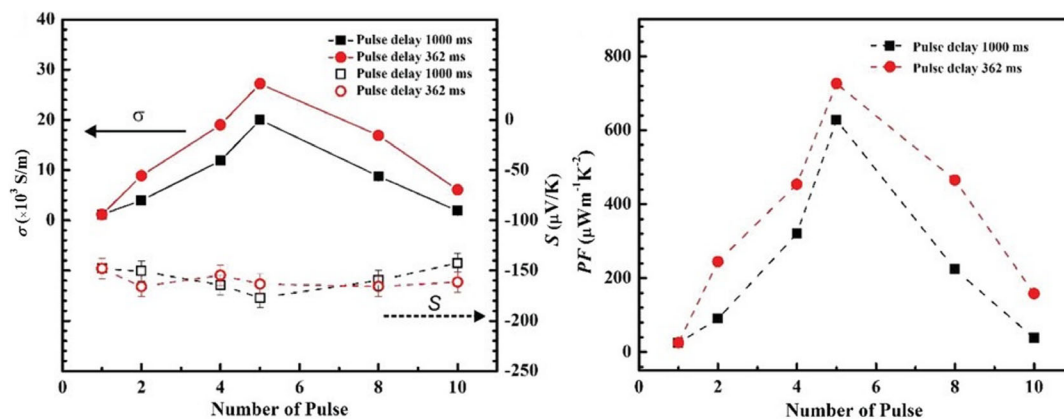**ADVANCED
ENGINEERING
MATERIALS**
www.aem-journal.com

Figure 8. The dependence of electrical conductivity and PF on the number of pulses for different pulse delays[107] (reproduced with permission, copyright 2019, John Wiley and Sons).
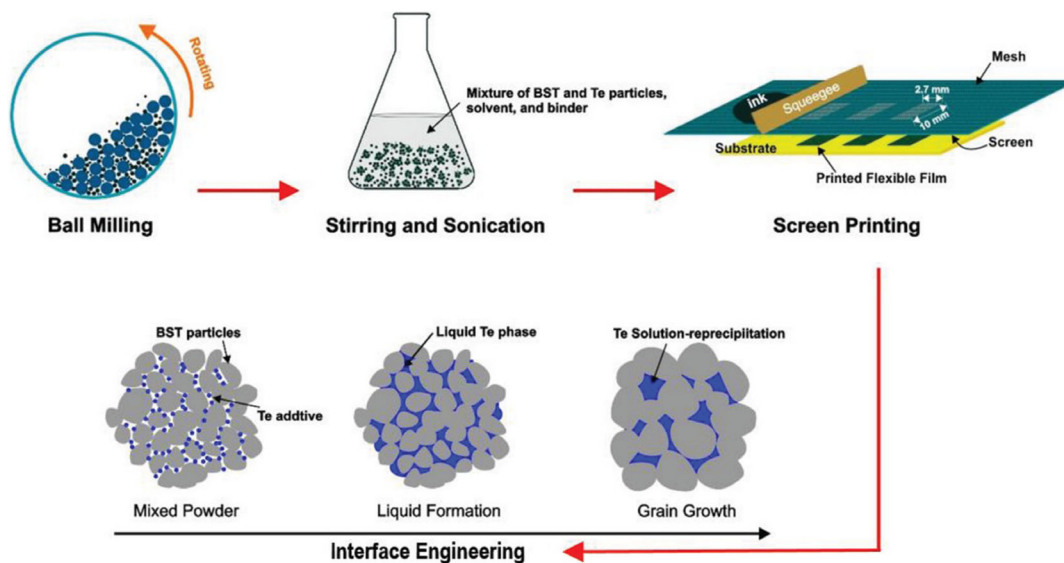

Figure 9. Schematic representation of the process of fabricating TEGs from BST particles and implementing nanosolder-assisted interface engineering[108] (reproduced with permission, copyright 2019, John Wiley and Sons).

with the BST:T sample. For α, both samples showed quite a decrease with temperature after an initial rise. But for BST:T, α started decreasing for temperatures above 423 K compared to 378 K for the pure BST sample. This is because of the reduction of the density of positively charged tellurium by the excess tellurium.[109] α decreased from 230 to 204 $\mu V\,K^{-1}$ as the temperature rose from RT to 498 K. The lattice κ in BST:T decreased due to the increase in phonon scattering due to the secondary tellurium phase. κ_L of BST:T was 0.620 $Wm^{-1}\,K^{-1}$, slightly lower than the BST sample with κ_L of 0.74 $Wm^{-1}\,K^{-1}$. The reported ZT value and PF in this work were comparatively better than most of the previously reported works like inkjet-printed BiSbTe film (PF:60 $\mu W\,m^{-1}\,K^{-2}$ at RT),[71] BiSbTe films made by dispersive printing (PF:180 $\mu W\,m^{-1}\,K^{-2}$ and ZT:0.2)[76] or p-type Bi_2Te_3/poly(3,4-ethyl-enedioxythiophene) film prepared with an evaporation method (power factor: 1350 $\mu W\,m^{-1}\,K^{-2}$ and ZT:0.58).[110] The second set of experiments was done with a Bi_2Te_3. By modifying the surface by

introducing nanosolder in a wide temperature range of 300–460 K, they achieved the highest PF of 363 $\mu Wm^{-1}\,K^{-2}$ (Figure 6b) and a ZT around 0.2.[68] Also, the influence of an inert gas like N_2 and a reducing atmosphere (Ar/H_2, 5% H_2 + 95% Ar) during the sintering process on the TE properties was investigated. The addition of Sb_2Te_3-based nanosolder minimized the change in electrical resistivity of the screen-printed film to under 3.6% after storage in the atmosphere for 6 months and increased durability against repeated bending. Nanosolder also helps grains to crystallize at a comparatively low temperature. Furthermore, it increases the density of the screen-printed films by filling the pores and promoting grain growth. In this process of producing TE films, it is important to deal with the porosity as surface oxidation degrades the power generation and service life of printed TEDs. This can be done by increasing the density of the printed films and reducing surface roughness. The results showed that the largest value of carrier concentration is $22.6 \times 10^{19}\,cm^{-3}$ for samples sintered with added nanosolder

being three times higher than that of the samples without nanosolder. The advantages and disadvantages of sintering at a reducing atmosphere (Ar/H$_2$) need to be considered. Sintering in Ar/H$_2$ atmosphere increases the porosity as well as the evaporation rate of Te, thus decreasing σ. Similarly, other TE properties like σ, α, and κ vary differently in different atmospheres with the change of temperature. The reducing atmosphere of Ar/H$_2$ increases α by allowing defect engineering.

This hot pressing helped the randomly oriented Bi$_{0.5}$Sb$_{1.5}$Te$_3$ grains rearrange along the (000 L) orientation during the curing process,[111] increasing σ. Thus, they reached the highest PF of 840 μW m^{-1} K^{-2} at 300 K when cured at 623 K, applying a pressure of 4 MPa (**Figure 10**a). This is 180% higher compared to the nonpressed film. Feng et al. showed in their recent results that electrical transport properties could be enhanced via defect engineering. For this purpose, they used a screen-printed Bi$_2$Te$_3$ ink mixed with Te-based nanosolder.[112] The surface morphologies depend on the amount of Te-NS in the ink, with the increase of TE-NS the surface porosity decreases. After drying at 673 K, the Bi$_2$Te$_3$ particles with no Te-NS in the film were much less sintered due to the higher sintering barrier. The addition of nanosolder favors the sintering by improving the surface energy allowing sintering below 673 K. As a result, the electrical conduction channel improved, resulting in a drastic rise of σ of about 7 times compared to the film without nanosolder. The particle size was small with high porosity. With 4 wt% Te-NS, they observed larger particles and tiny layer structures on the surface. Small grains replaced these layer structures if the amount of Te-NS was increased up to 8%. They found the least porous material with the largest particles with 12% Te-NS in the sample. σ also changed likewise, from a value of 3.71×10^3 S m^{-1} at 4 wt% of Te-NS to 31.57×10^3 S m^{-1} at Te-NS content of 12 wt%. With the further increase of the Te-NS content, the conductivity decreased, and the value got down to 24.63×10^3 S m^{-1} at 16% Te-NS content. This was because the mobility of the film started to decline at higher Te-NS content due to degradation of texture.[113] α at RT is the highest for the sample without Te-NS, 177.6 μV K^{-1}. It strictly decreased with the increasing amount of nanosolder. But the analysis of the temperature profile showed that without the inclusion of Te-NS, the α falls faster with the rise of the temperature than in the engineered samples and the trend

is monotonous with the increasing amount of Te content. This temperature-dependent α is determined by point defects. That is the reason p-type conduction occurs in the absence of Te-NS, whereas the film behaves like an n-type material due to the evaporation of the Te. Because of the change in intrinsic point defects caused by the evaporation of Te during the sintering process, p-type conduction occurs in the film without Te-NS, while n-type conduction occurs in films with Te-NS due to the compensation of evaporated Te. They achieved the highest PF with the sample with 12 wt% of Te-NS, 465 μW m^{-1} K^{-2} at 395 K (Figure 10b). Bismuth telluride nanoplates mixed with Polyvinylpyrrolidone (PVP) as a capping agent and ethylene glycol as a solvent also exhibit appreciable TE properties.[114,115]

Hollar et al. could achieve an appreciable PF of 350 μW m^{-1} K^{-2} at 433 K from a spin-coated Bi$_2$Te$_3$ ink on a polyimide substrate.[70] Here they observed an increase in σ from 1.8×10^4 to 2.9×10^4 S m^{-1} when the annealing temperature was increased from 573 to 673 K. With changing environmental temperature, α initially increased and reached its maximum value of 117 μV K^{-1} at around 410 K. They also performed a bending test as poor flexibility can greatly deteriorate σ. For spin-coated Bi$_2$Te$_3$, they observed the highest change in resistance of 17% with a 10 mm radius of curvature, and the change was smaller when the radius of curvature was 50 mm, 5%. While performing a dynamic bending test with a radius of curvature of 50 mm, the change in resistance increased from 13% to 23% as the number of the bending cycle went from 100 to 1000. Liu et al. performed a study of TE properties of boron-doped (0.1–0.5 at%) single-walled carbon nanotubes (B-SWCNTs).[116] The doping increased the α of the semiconducting SWCNTs to 32 μV K^{-1}. In theory, boron doping should reduce the electron conductivity of the individual SWCNTs, but they achieved a high conductivity of 214 000 S m^{-1} due to the improved electrical transport between laterally contacted metallic and semiconducting nanotubes leading to a PF of 226 μW m^{-1} K^{-2} at RT. Zeng et al. demonstrated that graphene-based materials could be used for TE energy harvesting as they could overcome the two major drawbacks of graphene through defect engineering. They achieved a high κ and a low α due to zero bandgap while maintaining its σ.[117] Considering the high cost and hazardous nature
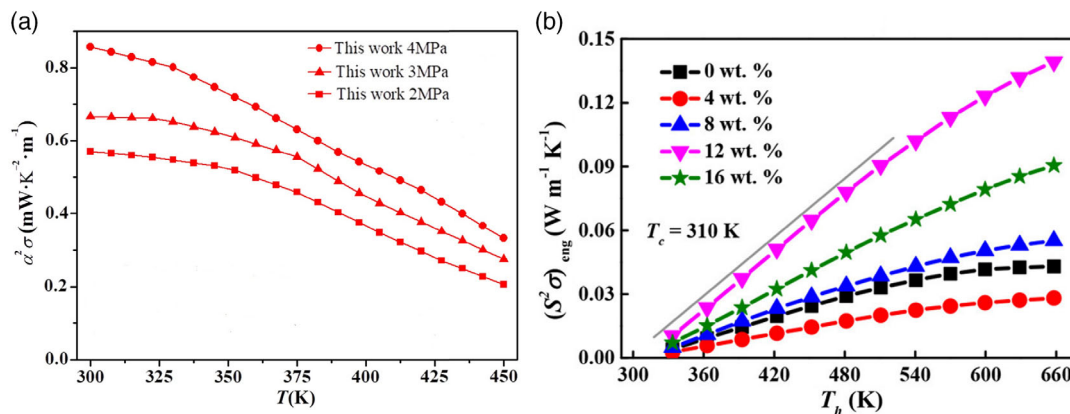

Figure 10. a) The effect of hot pressing on the PF as a function of temperature[152] (reproduced with permission, copyright 2018, Elsevier). b) is the dependence of device PF with different wt% of Te-NS[112] (reproduced with permission, copyright 2020, ACS publications).
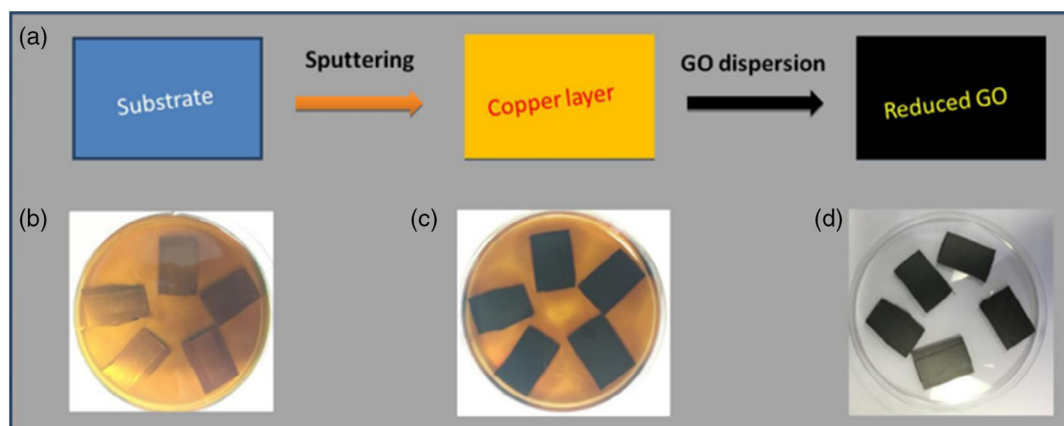
Figure 11. Schematic diagram of rGO fabrication. The images in the second row from the left are copper-coated PET substrate in the GO dispersion, copper reduced GO film in the GO dispersion, and copper-reduced GO film on the PET substrate, respectively[117] (reproduced with permission, copyright 2018, Elsevier).

of carbon nanotubes,[118,119] this can be a safer and cheaper option for energy harvesting. They deposited graphene oxide (GO) on copper-coated flexible material (**Figure 11**) and generated reduced graphene oxide (rGO) by a reduction mechanism. This led to a substantial in-plane reduction of κ from $2.0 \times 10^3 \, W \, m^{-1} \, K^{-1}$ in graphene to $2.96 \pm 0.02 \, W \, m^{-1} \, K^{-1}$ in the rGO sample. The effect was attributed to additional disorder induced phonon scattering. The restoration of the sp^2 carbon domains due to the self-healing effect and elimination of most of the oxygen-functional groups, rGO showed a couple of orders of magnitude increase of σ compared to GO, $1.43 \pm 0.03 \times 10^4 \, S \, m^{-1}$ at RT. The conductivity of rGO increases with the temperature till 323 K due to the variable

range hopping. α was also slightly higher ($18.4 \pm 2.16 \, \mu V \, K^{-1}$) than in pure graphene ($10–15 \, \mu V \, K^{-1}$). This might happen due to the different types of defects in their rGO. Combining all these TE properties, the ZT value and the PF were 4.88×10^{-4} and $5 \, \mu W \, m^{-1} \, K^{-2}$. This PF depends on the temperature and went above $8 \, \mu W \, m^{-1} \, K^{-2}$ at 323 K.

Recently, Ding et al. also used reduced-graphene oxide (rGO) nanosheets with bismuth telluride (Bi_2Te_3) nanoplates (**Figure 12**) to achieve good electrical properties and improved flexibility.[120] The amount of rGO was restricted to 1% as the p-type nature[121,122] of rGO compromises the α of the films which are n-type in nature.[103] But σ improved significantly with adding rGO due to a huge increase in electron mobility.
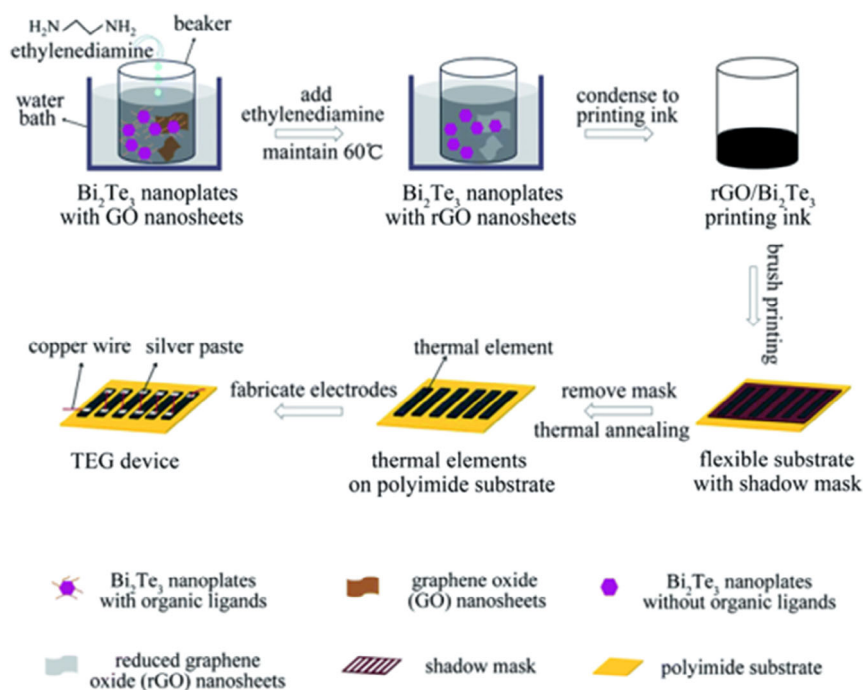

Figure 12. The printing process of a TED by rGO/Bi_2Te_3 ink[120] (reproduced with permission, copyright 2020, RSC).

This is because the rGO provides an extra transfer channel to electrons.[123]

The PF was the maximum for the sample with 1% rGO, 320 μW m^{-1} K^{-2} at 300 K and 460 μW m^{-1} K^{-2} at 400 K. The inclusion of rGO led to an increased κ. They calculated the ZT for the 1% rGO/Bi$_2$Te$_3$ material to 0.2 at 300 K and 0.4 at 400 K. In terms of the bendability, there was hardly any change in resistance after they bent the 1% rGO included sample with a bending radius between 4 and 6 mm. They observed a 2% increase in resistance for the 1% rGO/Bi$_2$Te$_3$ device when the bending radius was 5 mm, compared to the 10% increase for pure Bi$_2$Te$_3$ devices. The cause might be the fact that rGO helps to release the strain and improve flexibility.

Mallick et al. used Ag–Se-based n-type materials and prepared the films with a screen-printing method[124] (**Figure 13**a). They then sintered it at 573 K for 70 s. With the increasing percentage of Se ($\geq$30 at%) in the ink, σ measured at RT went down from 1.8×10^5 to 5.6×10^3 S m^{-1} due to the discontinuation of the Ag

percolation path. However, α increased with Se due to the formation of the Ag$_2$Se phase. The magnitude of the calculated α was higher than in the bulk Ag$_2$Se, 203.3 μV K^{-1} compared to 140 μV K^{-1}.[125] They could achieve a PF of $\approx$400 μW m^{-1} K^{-2} with 60 at% of Se in the composition, and the ZT value was $\approx$0.6 at 323 K (Figure 13b). They also found that the ink can be sintered at a lower temperature if given a greater sintering time, although the TE performance decreased due to the lower σ. They could even achieve a higher PF and ZT values of $\approx$1700 μW m^{-1} K^{-2} and 1.03, respectively, in another of their attempts with an improved ink[126] (Figure 13c). Here, the carrier concentration was found to go low with the increasing Se percentage in the composition as the excess volume fraction of Ag in Ag$_2$Se went down. σ varied from 5.0×10^4 to 1.0×10^4 S m^{-1} and the magnitude of α increased from 100 to 220 μV K^{-1} with the Se content. Optimum performance was measured when there were 27 at% of Se in the composition. Recently, they could demonstrate a record high ZT of around 1.2
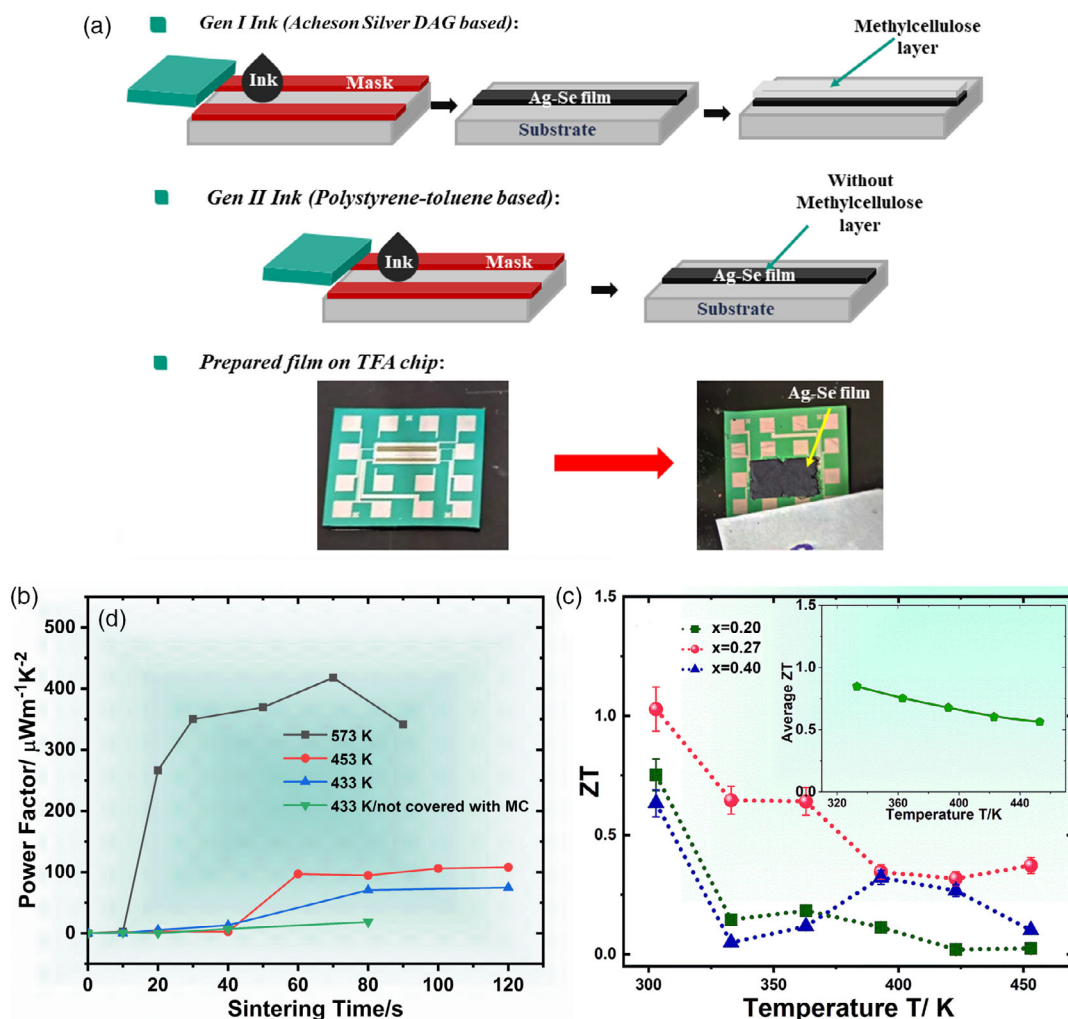

Figure 13. a) The sample preparation method for an Ag$_2$Se-based TEG[124] (reproduced with permission, copyright 2020, ACS publication). b) The PF and the ZT measurements as a function of temperature and the effect of sintering time and the sintering temperature on the PF[124] (reproduced with permission, copyright 2020, ACS publication). c) The ZT of the (1−x)Ag–(x)Se-based ink with different amounts of Se[126] (reproduced with permission, copyright 2020, RSC).

Table 1. Reported inorganic-based printed TE materials.

TE ink composition	Printing methods	Power factor [$\mu W\,m^{-1}\,K^{-2}$]	ZT max	References
n-type: Bi_2Te_3-epoxy	dispenser-printing	150 and 840 at RT	0.16 and 0.41 at RT	[73]
p-type: Sb_2Te_3 with 5 wt% toluene				
p-type: Sb_2Te_3	dispenser-printing	155 and 144 at RT	0.19 and 0.18 at RT	[40]
n-type: Bi_2Te_3				
n-type: mechanically alloyed (MA) Bi_2Te_3 with 1 wt% of Se	dispenser printing	470 at RT	0.31 At RT	[76]
p-type: Te-doped MA $Bi_{0.5}Sb_{1.5}Te_3$	dispenser printing	160 and 94 at RT	–	[42]
n type: Se-doped MA Bi_2Te_3				
p-type: mechanically alloyed (MA) $Bi_{0.5}Sb_{1.5}Te_3$ with 8% Te	dispenser printing	180 at RT	0.2 at RT	[86]
n-type: MA Bi_2Te_3 with 2 wt% Se	dispenser printing	150 at RT	0.17 at RT	[89]
p-type: $Bi_{0.5}Sb_{1.5}Te_3$ with 8 wt% Te	dispenser printing	80 at RT		[41]
n-type: Bi_2Te_3	screen printing	2100 at RT	0.61 at RT	[30]
p-type: $Sb_{1.5}Bi_{0.5}Te_3$ NPs	inkjet printing	77 and 183 at 348 K	–	[71]
n-type: $Bi_2Te_{2.7}Se_{0.3}$ NPs				
n-type: Bi2Te3	screen printing	–	0.43 at 448 K	[28]
p-type: $Bi_{0.5}Sb_{1.5}Te_3$	screen printing	–	0.68 and 0.81 at RT	[93]
n-type: $Bi_2Te_{2.7}Se_{0.3}$				
p-type: $Bi_{0.7}Sb_{1.3}Te_3$ with 4% Pb	solution process	1150 At 500 K	1 at 513 K	[101]
n-type: $Bi_2Te_{2.8}Se_{0.2}$ NP	screen printing	30 at 473 K	–	[104]
n-type: $Bi_2Te_{2.7}Se_{0.3}$	3D Conformal Printing	730 at RT	–	[107]
p-type: $Bi_{0.4}Sb_{1.6}Te_3$ with 8% tellurium	scalable printing	3000 at RT	1 at RT	[108]
n-type: Bi_2Te_3	screen printing	363 at 370	0.25 at 370 K	[68]
p-type: $Bi_{0.5}Sb_{1.5}Te_3$	brush-printing	840 at RT	–	[152]
n-type: Bi_2Te_3 with 12% Te-Ns	screen printing	465 at 395 K	–	[112]
n-type: Bi_2Te_3	solution-processed colloidal NP	350 at 433 K	–	[70]
p-type: boron-doped single-walled carbon nanotubes	ink printing	226 at RT	–	[116]
rGO	3D printing	8 at 423 K	$4.88 \times 10{-4}$	[117]
n-type: Bi_2Te_3 nanoplates with 1% rGO	printing	460 at 400 K	0.4 at 400 K	[120]
n-type: Ag_2Se	screen printing	400 at 323 K	0.6 at 323 K	[124]
n-type: Ag_2Se	screen printing	1700 at RT	1.03 at RT	[126]
p-type: S-substituted β-Cu_2-δSe	screen printing	250 at RT	0.15 at RT and 0.21 at 375 K	[55]
p-type $Bi_{0.5}Sb_{1.5}Te_3$	screen printing	1750 at RT	1.2 at RT	[127]

at RT with $Bi_{0.5}Sb_{1.5}Te_3$-based printable TE ink through grain interface modification by an in situ-grown β–$Cu_{2-\delta}$Se phase. The reported PF is around $1.750 \times 10^3\,\mu W\,m^{-1}\,K^{-2}$.[127] Apart from these, there are other reports where AgS-based ink doped with Te and Se showed good mechanical properties[128,129] and high ZT value up to 0.44 at 300 K making them good candidates for flexible TE applications.[130,131] **Table 1** can be referred to as a summary of the PFs and the ZT values of recently reported inorganic-based printed TE materials.

5. Inorganic–Organic Hybrid Printed TE Materials

Chalcogenides such as bismuth telluride and antimony telluride as bulk materials are known as high-performance TE materials for RT applications. However, developing a printable TE material for use in flexible devices based on these chalcogenides is not

easy. The transition from bulk to printed materials poses a serious challenge for maintaining a high σ. Moreover, mechanical flexibility is another significant challenge. On the other hand, polymeric semiconductors exhibit good flexibility and printability. However, they show inferior TE performance. Therefore, efforts are put forward to synthesize inorganic-based TE printed materials and hybridize them with conducting polymers such as PEDOT:PSS. We et al. used a screen-printing technique to prepare inorganic–organic thick TE films.[132] The inorganic ink was prepared with 75% of metal powders like Bi, Sb, and Te, 0.2% of binder, 2.4% of glass powder, and 22.4% of solvent in their weight compositions. They used the glass powder to increase the adhesion between the paste and the substrate to avoid delamination after annealing. They screen printed the obtained ink on flexible PI substrates followed by annealing it at 473 K. They used PEDOT:PSS with 5 vol% of DMSO to infiltrate into the micropores of the screen-printed TE thick films which were generated
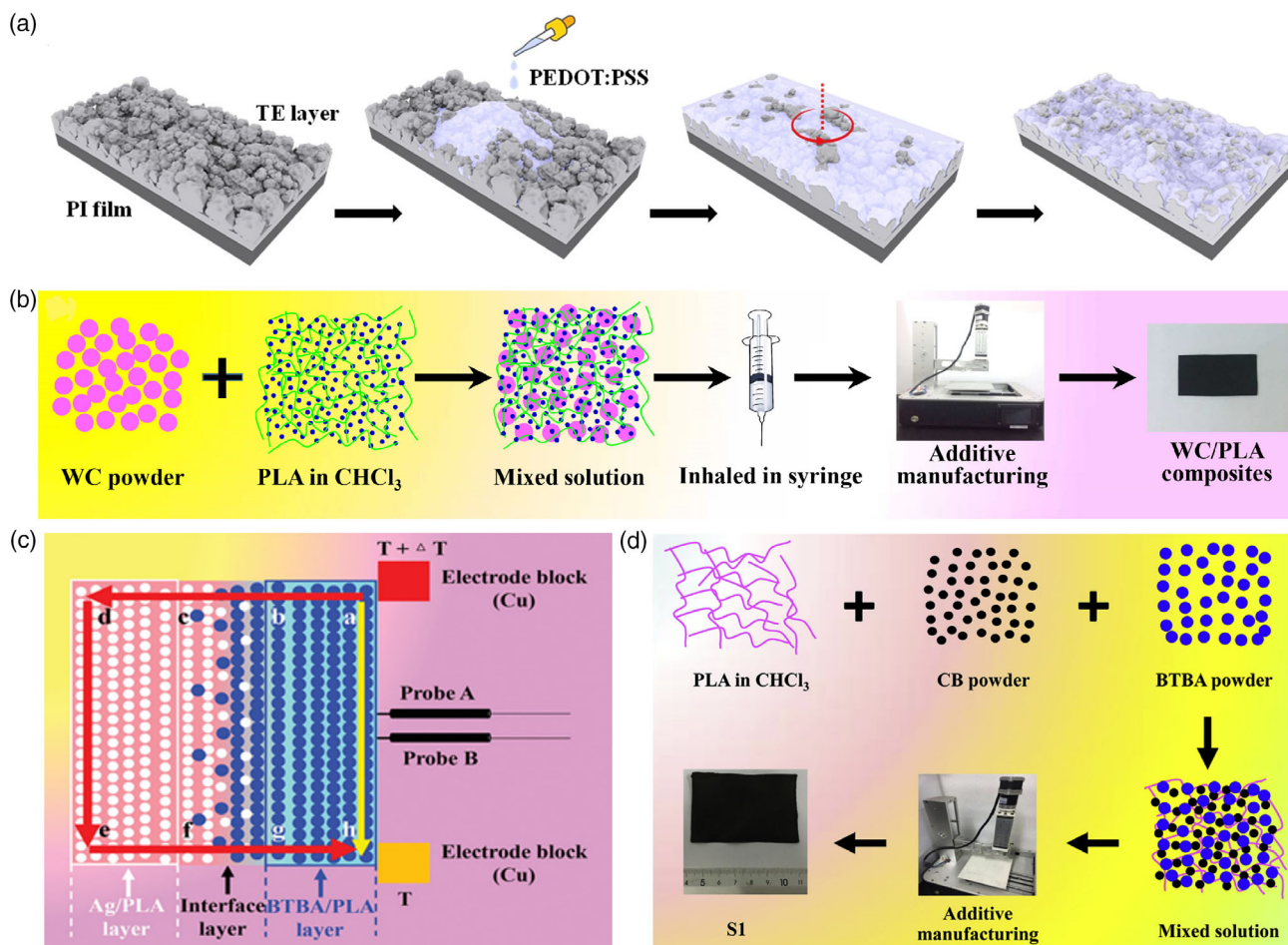
Figure 14. a) The morphology of the printed Bi_2Te_3 ink before and after the infiltration of PEDOT:PSS[132] (reproduced with permission, copyright 2014, Elsevier). b) The schematic flow chart of the fabrication process of the WC/PLA thermoelectric composites, respectively[72](reproduced with permission, copyright 2018, MPDI). c) The illustration of the transport mechanism of the charge carriers in the double-layer inorganic/organic composites synthesized by additive manufacturing[146](reproduced with permission, copyright 2020, John Wiley and Sons). d) The schematic representation of fabricating CB/BTBA/PLA composites by additive manufacturing[148](reproduced with permission, copyright 2020, Elsevier).

due to the evaporation of the solvent and organic binder during the annealing process (**Figure 14**a). These pores weaken the mechanical strength as well as lower σ. The inclusion of PEDOT:PSS had its impact on both, the TE and the mechanical properties. The results indicated that the carrier concentration of the screen-printed TE thick films increased by 9–14% due to the addition of high conductive PEDOT:PSS. As a result, they observed an increase of 10% in ZT after the PEDOT:PSS infiltration process for both p- and n-type TE materials. The highest values they reported were 0.2 (p-type) and 0.16 (n-type) at RT. Apart from improving the ZT, PEDOT:PSS also improved the flexibility of the printed films. The results revealed that PEDOT:PSS infiltrated samples could maintain the resistance up to a bending radius of 3 cm for both materials. But without PEDOT:PSS, the resistances increased more than 2.5 folds for the same bending radius. Du et al. fabricated n-type tungsten carbide/polylactic acid (WC/PLA) composites by additive manufacturing[72] (Figure 14b). They prepared the initial solution by mixing 0.8 g of PLA in 12 mL of chloroform and then WC powder was mixed in different ratios. Though the TE properties

improved as the amount of WC increased, the ink loses its flexibility. σ increased from around 1000 to 42 000 S m⁻¹ at ≈300 K (nominal volume ratios of WC in the considered samples were ≈33%, 50%, and 60%, respectively). WC/PLA has a higher σ compared to most of the previously reported n-type polymers, such as 62 S m⁻¹ for ClBDPPV combined with 25 mol% tetrabutylammonium fluoride,[133] 23 S m⁻¹ for 1-ethyl-3-methyl-imidazolium ethyl-sulfate-doped polyaniline,[134] and 50 S m⁻¹ for PVDF/DMSO on paper.[135] α, however, does not vary drastically and stays between −10.3 and −12.5 µV K⁻¹ in the temperature range from 150 to 375 K. The compound with 60% WC exhibited a maximum PF of 0.64 µW m⁻¹ K⁻² at 250 K and decreased slightly for higher temperatures. The κ of the composites was much lower than that of WC (29–121 W m⁻¹ K⁻¹) as the surface of the WC particles was coated by PLA. At 300 K, it varied from ≈0.20 to ≈0.28 W m⁻¹ K⁻¹ for different WC concentrations. Using this approach, they achieved the highest ZT value of ≈6.7×10^{-4} at 300 K. The flexibility was also reasonable as the electrical resistance for the samples containing ≈33% WC only increased by 6.6%, after being bent 300 times with different radii,

100 times at 13, 100, and 8.1 mm each, respectively. Furthermore, they found no appreciable change in α. They demonstrated that nanostructuring could result in improving ZT values of the bulk TE materials.[88,136–139] A novel hybrid organic–inorganic nanocomposite structure has benefits like intrinsically low κ polymeric matrix due to the hindered thermal transport caused by the large thermal interface resistance at the interfaces.[135,140,141]

Ou et al. investigated the effects of adding Bi_2Te_3/Sb_2Te_3 nanocrystals in PEDOT:PSS-based inks.[142] The TE films were printed using aerosol jet printing. The films were printed on a polyimide substrate and possessed thermal stability up to 673 K. They also showed an excellent performance in bending tests with curvatures up to 300 m^{-1}. By controlling the Bi/Te and Sb/Te ratio in the precursor solution, they could produce a Bi- or Sb-rich ink providing a higher concentration of holes and exhibiting p-type properties or vice versa. The sample for the experiment contained 41.1 at% of Bi slightly above the concentration expected for a stoichiometric compound. They observed that the TE properties, mechanical stability, and homogeneity highly depended on the chemical treatment and the number of printed layers. Here, the highest σ and the PF were from EG-treated samples with five-layer printing. α could also be controlled by changing the loading ratio between the organic and the inorganic components. But they found a slight decrease in σ with the increase in wt% of Bi_2Te_3 or Sb_2Te_3 nanocrystals, although α improved. With increased loading, the peak value of $\alpha \approx 36.6\,\mu V\,K^{-1}$ was achieved, which was higher compared to the PEDOT:PSS film with α of $\approx 17.1\,\mu V\,K^{-1}$. Keeping in mind that the loading shows opposite impacts on α and σ, determining an optimum value is important. For p-type PEDOT:PSS-based nanocomposites, they achieved the best performance at 85 wt% of Sb_2Te_3, with an α of $\approx 33.8\,\mu V\,K^{-1}$, σ of $\approx 2.473 \times 10^4\,S\,m^{-1}$, and a PF of $\approx 28.3\,\mu W\,m^{-1}\,K^{-2}$ at RT. These values obtained via aerosol jet printing were comparable to previously reported values based on other printing techniques.[37,140,143–145] Though sintering at elevated temperatures could improve the TE properties, it was not possible due to the presence of the polymer substrate. The results were also auspicious when it came to mechanical stability and bendability. Du et al. demonstrated that the power factor could also improve by combining composite layers of different transport properties.[146] They synthesized one layer with a high σ and another with a high α by a solution additive manufacturing process. These layers were made of Bi_2Te_3-based-alloy/polylactic acid (BTBA/PLA) and Ag/PLA composites. They were able to manipulate σ of these double-layer composites by changing the amount of Ag and could increase it from 1.2×10^3 to $11.7 \times 10^4\,S\,m^{-1}$ by increasing the volume ratio of Ag from 26.3% to 41.7% in the Ag/PLA layers. This happened due to the contribution of the higher σ of Ag[147] while the α remained constant $\approx 80\,\mu V\,K^{-1}$ at 300 K. It is possible to have a σ of 171 000 S m^{-1} by further increasing the volume-ratio of Ag to 45.6%. The reason for having such high σ is that holes choose the indirect path through the high conducting Ag/PLA layer when connected to a constant heat source. In the schematic illustration (Figure 14c), the current flows the longer path $a \to b \to c \to d \to e \to f \to g \to h$ over the direct path $a \to h$ due to the difference of σ between Ag/PLA and BTBA/PLA layer.

Here they observed a slight decrease of α to 64 $\mu V\,K^{-1}$. They obtained a PF of 875 $\mu W\,m^{-1}\,K^{-2}$ at 360 K with a vol% of 41.7 Ag in the Ag/PLA layers. The high α is the result of the scattering of charge carriers at the graded interfaces, along the route $a \to b \to c \to d \to e \to f \to g \to h$. For single-layer composites, the highest α they observed was for the BTBA/PLA layer with a BTBA volume ratio of 39.6%, which varied from 185 to 205 $\mu V\,K^{-1}$ in a temperature range from 300 to 345 K, way higher than the double layer. But for the Ag/PLA single-layer composites, the α was as low as 1 $\mu V\,K^{-1}$ regardless of the volume ratio of Ag. The highest PF for single-layer composites that they could obtain for BTBA/PLA layer was 2.2 $\mu W\,m^{-1}\,K^{-2}$ at 345 K and was much lower than the composite layer where the PF is around 875 $\mu W\,m^{-1}\,K^{-2}$ at 360 K with 39.6% volume ratio of BTBA and with 41.7% Ag volume.

The same group also demonstrated that flexible ternary carbon black/Bi_2Te_3 based alloy/polylactic acid (CB/BTBA/PLA) composites enhance the TE properties of the ink.[148] They also produced it by an additive manufacturing process (Figure 14d). By increasing the mass ratio of BTBA from 38.5% to 71.4% at 300 K, they achieved an increase in α, from 60.2 to 119.9 $\mu V\,K^{-1}$. σ also changed from 580 to $1.33 \times 10^3\,S\,m^{-1}$. As a result, the PF of the composites significantly increased from 2.1 to 19.2 $\mu W\,m^{-1}\,K^{-2}$, and the ZT value increased by 575%, from 0.004 to 0.023. This optimum ZT value was recorded at 320 K and with a 71.4 wt% of BTBA in the composite. They obtained an even better result by using Bi_2Te_3-based alloy nanosheet/poly(3,4ethylenedioxythiophene):poly(4-styrenesulfonate) (PEDOT:PSS) composite films produced separately by spin coating (1000 rpm for 60 α followed by 2000 rpm for 60 s) and drop-casting techniques.[144] They observed that the σ of the drop cast composites was way higher than one of the spin-coated composites, which in turn gives a higher PF for the spin-coated composites as well. This was attributed to the nanometer grain size and the rougher surface of spin-coated composites.[138] The drop cast composite film had the highest σ of $129.520 \times 10^3\,S\,m^{-1}$ when the BST nanosheet content was 4.10 wt%. The highest value for α was 47.5 $\mu V\,K^{-1}$ when the concentration of BST nanosheets was 9.65 wt% in the spin-coated composite films. Spin-coated films showed a huge increase in PF in the proportion of BST NSs content. This was obvious due to the increased α. For the drop cast composite, the PF kept increasing until the BST nanosheet content reached 4.10 wt% and then remained unchanged. This can be attributed to the balance between the decrease of σ after a sharp increase and the gradual increase of the α. They reached a maximum PF of 32.26 $\mu W\,m^{-1}\,K^{-2}$ for the drop cast composite film with a 4.10 wt% BST NSs. Pires et al. demonstrated that, if Bi_2O_3 present on the surface of the Bi_2Te_3 microparticle is reduced by an HCl treatment, it improves the TE properties of the film.[69] They could achieve an optimum balance between the homogeneity of the ink and the performance of the ink was produced with 25 wt% of PVA and 75 wt% of chemically treated Bi_2Te_3 micro powder with a RT PF of 0.04 $\mu W\,m^{-1}\,K^{-2}$ and an α of $-166\,\mu V\,K^{-1}$. The chemical treatment in the absence of PVA samples led to a PF of 2.29 $\mu W\,m^{-1}\,K^{-2}$, twice as compared as the untreated samples. For the sample prepared by solid-state reaction (SSR), the PF varies from 0.01 to 1.24 $\mu W\,m^{-1}\,K^{-2}$ depending on the amount of PVA. Altogether, they achieved the best ZT

(0.0013) when they treated the sample chemically compared to the untreated one (ZT = 0.0006), as the chemical treatment increased the σ up to 45% without affecting α and κ. They could also show that the ratio of PVA to Bi_2Te_3 had an impact on the TE properties. With a very high percentage of Bi_2Te_3 (PVA:Bi_2Te_3_(SSR) = [10:90]) they achieved a very low porosity, however, the samples revealed visible microcracks which can easily cause peeling of the film from the substrate. Therefore, it is safe to have a Bi_2Te_3 concentration of less than 80% to have a mechanically stable film. Analyzing the results for an ink of 75% Bi_2Te_3 yielded the highest PF while maintaining mechanical stability. Kato et al. applied the screen-printed method to prepare such composite films.[149] The ink consisted of Bi_2Te_3 particles, polyimide with ionic liquid, and PEDOT:PSS. They annealed the films at 673 K for 1 h in an argon and hydrogen atmosphere. For the p-type materials, α, σ, and κ were 245 $\mu V\,K^{-1}$, $1.6 \times 10^4\,S\,m^{-1}$, and 0.33 $W\,m^{-1}\,K^{-1}$, respectively. For the n-type material, values of $-165\,\mu V\,K^{-1}$, $1.4 \times 10^4\,S\,m^{-1}$, and 0.23 $W\,m^{-1}\,K^{-1}$ were found. The maximum PF and the ZT calculated for the p- and the n-type were 960, 350 $\mu W\,m^{-1}\,K^{-2}$, and 0.87 and 0.5, respectively at RT. We summarize some of the properties of recently reported printed TE hybrid ink in **Table 2**.

6. Printed TEDs

TEDs have a basic structure where the n- and the p-type elements are connected in series in an alternating sequence so that the generated voltage by each component adds up. The number of components depend on the output requirement and the application. **Figure 15** shows schematic sketches of TEDs, fabricated TEGs of different shapes and sizes, and some laboratory demonstrations.

Kim et al. fabricated a flexible TEG using the screen-printing technique on glass fabric (**Figure 16**a). They studied the flexibility of the device by bending it with a radius of 20 mm and demonstrated a steady performance even after bending for 120 cycles.[150] They fabricated printed films with 8 thermocouples of n-type Bi_2Te_3 and p-type Sb_2Te_3 with a dimension of 15.0 mm × 20.0 mm × 0.5 mm and achieved an open-circuit voltage of 90 mV at a $\Delta T = 50$ K and a high-power density

of $3.8 \times 10^3\,\mu W\,cm^{-2}$. They stressed the lightweight properties of their device and reported a power output of $28 \times 10^3\,\mu W\,g^{-1}$. Moreover, the output power for the device on glass fabric was higher than on Al_2O_3 substrates as the fabric leads to a lower thermal resistance.

Rösch et al. used screen printing followed by a folding process to fabricate a TEG (as shown in Figure 16b) with TE inks based on PEDOT nanowires for the p-type legs and a TiS_2:hexylamine-complex material for the n-type legs. They realized a power output of 47.8 $\mu W\,cm^{-2}$ at a temperature difference of 30 K.[151] The device consisted of 254 p- and 253 n-legs on a checkerboard pattern of 13 columns and 39 rows with an area of 10.62 mm × 4.17 mm for each leg. In their experiment, they used the substrate as an insulating layer between the TE elements using a folding technique allowing a very thin spacing between the TE legs, essentially the substrate thickness of 6 μm. As a result, they achieved a high density of thermocouples, of around 190 cm^{-2}, which generated a high open-circuit voltage. We et al. also adopted the screen-printing process to fabricate a TEG using Sb_2Te_3 and Bi_2Te_3 nanoparticles, which were infiltrated afterward with PEDOT:PSS 5 vol% of DMSO.[132] DMSO helps to improve the σ of the material. They demonstrated that the area ratio of the printed n- and p-type TE legs (A_n and A_p) has an impact on the performance of the TEDs as they have different thermal and electrical properties (Figure 16c). They achieved an optimum output power density of 1200 $\mu W\,cm^{-2}$ at a 50 K temperature difference with a hot side temperature of 333 K when the ratio of A_n to A_p was 3. Here, the printed TEG consisted of 7 thermocouples and a polyimide film as a flexible substrate while they used a screen-printed Ag film as an electrode. Their fabricated device with 15 TE couples could generate a voltage of 12.1 mV with human body heat (Figure 16d). Kato et al. achieved a maximum power output of 200 μW at a temperature difference of 43 K in a 5 cm × 5 cm screen-printed TEG. They used n- and p-type hybrid Bi_2Te_3-polyimide ink mixed with an ionic liquid for fabricating the TEG.[149] Pires et al. used a chemically (HCl) treated hybrid Bi_2Te_3/PVA composite to prepare a screen-printed TEG of 10 stripes with 0.2 cm × 2.5 cm each. The TEG exhibited a power output up to ≈9 $\mu W\,cm^{-2}$ with a 46 K temperature difference.[69] Javas et al. demonstrated a power density of 2700 $\mu W\,cm^{-2}$ when

Table 2. Reported inorganic–organic hybrid printed TE materials.

TE ink composition	Printing methods	Power factor [$\mu W\,m^{-1}\,K^{-2}$]	ZT max	References
p-type: Sb_2Te_3 n-type: Bi_2Te_3 and PEDOT:PSS with 5 vol% of DMSO	Screen printing	–	0.2 (p-type) and 0.16 (n-type) at RT	[132]
n-type: tungsten carbide/polylactic acid (WC/PLA)	Additive manufacturing	0.64 at 250 K	$6.7 \times 10-4$ at 300 K	[72]
p-type: Bi_2Te_3/Sb_2Te_3 nanocrystals with PEDOT:PSS	Aerosol jet printing	28.3 at RT	–	[142]
p-type: Bi_2Te_3-based-alloy/polylactic acid (BTBA/PLA) and of Ag/PLA p-type ink	Additive manufacturing	875 at 360 K	–	[146]
p-type : ternary carbon black/Bi_2Te_3 based alloy/polylactic acid (CB/BTBA/PLA) p-type ink	Additive manufacturing	19.2 at 320 K	0.023 at 320 K	[148]
n-type: Bi_2Te_3/PVA treated with HCL	–	2.29 at RT	0.0013 at RT	[69]
p-type: Bi_2Te_3 particles n-type: polyimide with ionic-liquid	screen printing	960 and 350 at RT	0.87 and 0.5 at RT	[149]

Figure 15. a) A typical schematic representation of a TED connected electrically in series and thermally in parallel[74] (reproduced with permission, copyright 2006, Elsevier). b) A flexible TED prepared by B-SWCNTs[116] (reproduced with permission, copyright 2020, ACS publication). c) Four different images where the ink, the fabricated TEG, the integration of the TEG on the hand and the practical demonstration of the device are shown.[124] d) The high open-circuit voltage of 72.2 mV of the device[124] (reproduced with permission, copyright 2020, ACS publication). e) is the 3D printed TEG unit made of rGO and the thermal infrared image of the wearable device consisting of multiple such units[117] (reproduced with permission, copyright 2018, Elsevier). f) The cross-sectional image of screen-printed n-type Ag_2Se and the printed TEG with two thermocouples during operation[126] (reproduced with permission, copyright 2020, RSC). g)[41] (reproduced with permission, copyright 2014, API publication), and h)[42] custom-built TEDs with different shapes and sizes and i)[42] is a set-up for output measurement (reproduced with permission, copyright 2015, Elsevier).

the temperature difference between the hot and the cold side of a printed TEG was 50 K.[107] They used aerosol jet-printed $Bi_2Te_{2.7}Se_{0.3}$ films to fabricate the TEG. They also experimented with ball-milled $Bi_{0.4}Sb_{1.6}Te_3$ NPs and tellurium-based nanosolder. The screen-printed device with four BST:T legs

gave a much improved power density of 1880 µW cm^{-2} with a temperature difference of 80 K.[108] Feng et al. also used Bi_2Te_3 ink with 12 wt% Te-based nanosolder to make their device.[112] It was screen printed and the dimensions were 10 mm × 5 mm × 166 µm. They received a maximum output
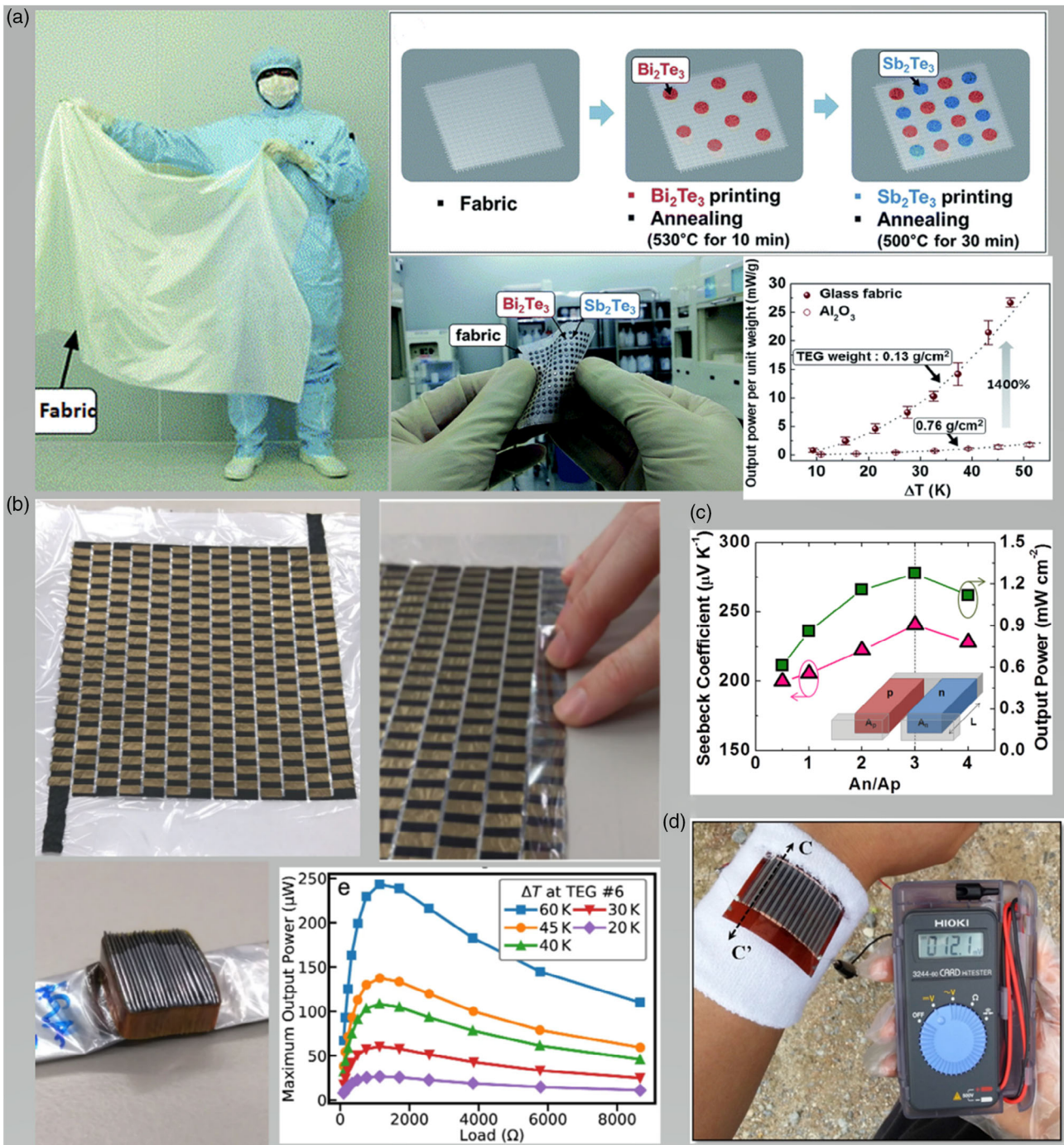
Figure 16. a) The commercial glass fabric, the fabrication process of the TEG, and the output power generated per unit weight[150] (reproduced with permission, copyright 2014, RSC). b) The folding process of the printed 2D TEGs and the output power as a function of electrical load at different temperature differences[151] (reproduced with permission, copyright 2021, Elsevier). c) The impact of the area ratio of n- and p-type legs on the TE properties[132] (reproduced with permission, copyright 2014, Elsevier). In d), a demonstration of a TEG with 15 TE couples is shown where the temperature difference between the human body and the ambient could generates a voltage of 12.1 mV[132] (reproduced with permission, copyright 2014, Elsevier).

power density of 3.265×10^3 $\mu W\,cm^{-2}$ (maximum power output was 27.1 μW) at a temperature difference of 105 K. Ding et al. used reduced-graphene oxide (rGO) nanosheets with bismuth telluride (Bi_2Te_3) nanoplates as ink to fabricate a printed TEG.[120] The highest power output of 1.72 μW at $\Delta T = 20$ K

was received when the relative concentration of rGO in the ink was 1%. Any addition or reduction of rGO resulted in a reduced output of power. Chen et al. fabricated TEGs in a mm scale and reported a power output of 10.5 μW by a printed TEG at a temperature difference of 20 K with a power density of
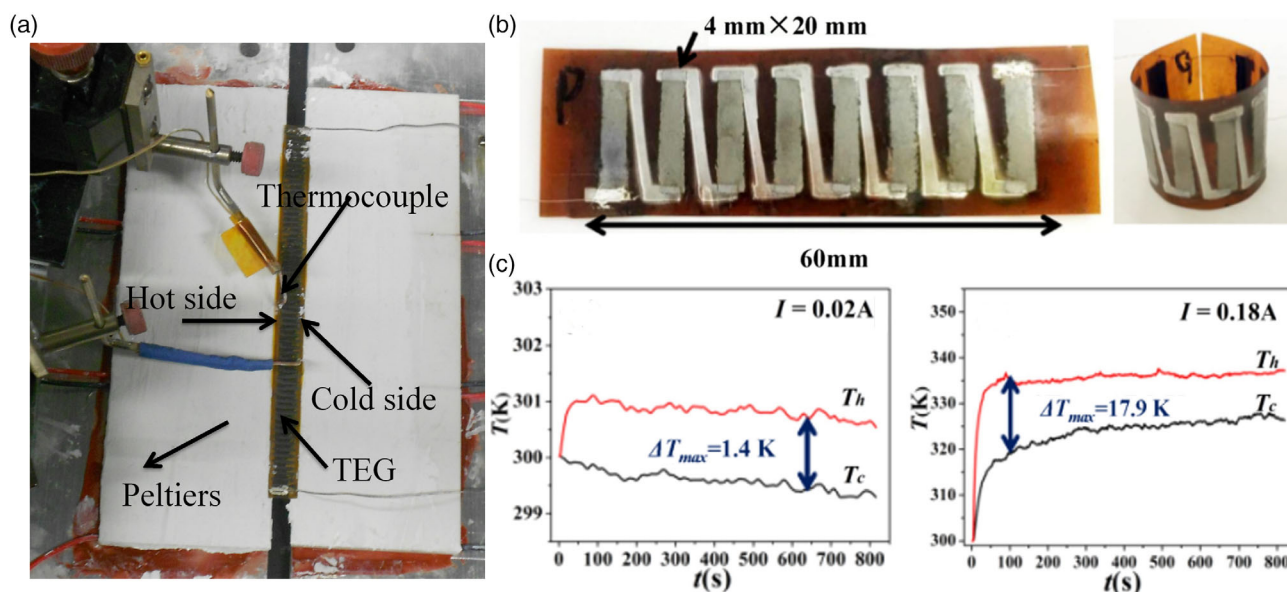
Figure 17. a) The custom-built characterization set-up with a 62-element TEG made of MA Bi_2Te_3 with 1 wt% extra Se[76] (reproduced with permission, copyright 2012, ACS publication). b) TE cooling device made of $Bi_{0.5}Sb_{1.5}Te_3$/epoxy thick films, and c) The temperature difference achieved as a function of time with different applied currents[152] (reproduced with permission, copyright 2018, Elsevier).

75 μW cm^{-2}.[40] They used p-type Sb_2Te_3 and n-type Bi_2Te_3 inks to realize a TEG using dispenser printing on a polyimide substrate. They achieved a higher output of 130 μW cm^{-2} with a 62 single-legged printed TEG prototype (**Figure 17**a) with 5 mm × 700 μm × 120 μm dimensions at the same temperature difference using mechanically alloyed n-type Bi_2Te_3-epoxy composite films with 1 wt% Se.[76] Varghese et al. synthesized an n-type Bi_2Te_3 based ink and used the same to fabricate a printed TEG using the screen-printing method.[28] A power output density of 4100 μW cm^{-2} with a 60 K temperature gradient was attained. The TEG consisted of 5° n-type legs and had a cross-sectional area of 2 mm × 0.01 mm for each of them.

Hou et al. prepared a cooling device (Figure 17b) and reported a maximum temperature difference of 1.4 K when the applied current was 0.02 A.[152] When the current increased to 0.06 A, they achieved a difference of 6.2 K between the hot and the cold side. The highest outcome was 17.9 K at a current of 0.18 A. They find that the temperature difference between the hot and the cold side is greatly affected by the Joule heating effect caused by the internal resistance of the device. As shown in Figure 17c, the temperature of the cold side decreases when the applied current is low, and the Peltier effect is dominant. But when a high current was applied, more heat was generated due to Joule heating and the Fourier effect. As a result, the temperature of the cold side started increasing, and no net cooling of the cold side was observed. The performance of various printed TEDs is shown in **Table 3**.

7. Challenges and Future Roadmap

Despite remarkable advancement in printed TE materials in the past decade, the efficiency of the printed TE devices is still not in accordance with the performance of the used materials. High electrical and thermal contact resistances are two main reasons of exhibiting lower conversion efficiency on the device level. In addition, although few reports show good printability and mechanical properties, most TE inks do not hold those qualities up to the mark.[153,154] Improving the mechanical as well as the TE properties of the printed films at the same time is one of the biggest challenges. Simplifying the preparation process is another hurdle to overcome. Solid-state processing at elevated temperature allows a well-controlled chemical composition and better compaction but is poor in terms of morphology.[155] Also, the polymer substrates decompose at higher temperatures.

Further extensive studies on device architectures and electrical and thermal contacts are required to improve the conversion efficiency of printed TE devices. The additional research on the different high-efficiency bulk materials to make them printable could lead to new kinds of high-efficiency printed TE materials. New effective fabrication methods could also be employed to improve the performance and robustness of the TE devices. Recently, the photonic curing[156] process is found to be a very promising sintering process that facilitates high performance and good mechanical flexibility without damaging polymer substrates. As the process takes just a few milliseconds to sinter the printed TE materials, it also minimizes the chance of oxidation. In addition, the conversion efficiency depends on the geometry of the TE devices as it controls the electrical and thermal impedance of the devices.[157] The role of geometry on device performance is another important area of study. For ink preparation, the solution-based wet chemistry method is one of the promising synthesis routes as it helps improve the surface chemistry of the ink.[158] Appreciable results from TE inks[159,160] and printed devices[161–166] prepared with different compositions and different recipes have been reported in recent times, but extensive research on the same is needed to overcome

Table 3. Performance of printed TEDss.

TE legs	Printing methods	Power output, μW [μW cm^{-2}]	Temperature difference ΔT [K]	References
p-type: Sb_2Te_3 n-type: Bi_2Te_3	Dispenser printing	75 μW cm^{-2} (10.5 μW at 171.6 mV)	20	[40]
n-type: Bi_2Te_3/PVA	–	9 μW cm^{-2}	46	[69]
n-type : Se-doped Bi_2Te_3	Dispenser printing	135 μW cm^{-2}	20	[76]
p-type: $Bi_{0.5}Sb_{1.5}Te_3$, n type: Se-doped Bi_2Te_3	Dispenser printing	280 μW cm^{-2}	20	[42]
n-type: Se-doped Bi_2Te_3	Dispenser printing	25 μW cm^{-2}	20	[89]
$Bi_{0.5}Sb_{1.5}Te_3$/Te	Dispenser printing	1230 μW cm^{-2}	70	[41]
n-type: Bi_2Te_3	screen printing	4100 μW cm^{-2}	60	[28]
n-type: $Bi_2Te_{2.7}Se_{0.3}$	3D Conformal Printing	2700 μW cm^{-2}	50	[107]
p-type: $Bi_{0.4}Sb_{1.6}Te_3$/Te	Screen printing	18 800 μW cm^{-2}	80	[108]
p-type: $Bi_{0.5}Sb_{1.5}Te_3$	Brush printing	Cooling device, 6.2 K under the working current of 0.06 A		[152]
n-type: Bi_2Te_3/Te-NS	Screen printing	3265 μW cm^{-2}	105	[112]
p-type: B-doped SWCNTs	Ink printing	0.40 μW at 20 mV	60	[116]
n-type: Bi_2Te_3/r-GO	Doctor blading	1.72 μW	20	[120]
n-type: Ag_2Se	Screen printing	321 μW cm^{-2}	110	[124]
n-type: Ag_2Se	Screen printing	0.19 μW	60	[126]
p-type: S-substituted β-$Cu_{2-δ}Se$ n-type: Ag_2Se	Screen printing	0.32 μW	45	[55]
p- and n-type: Bi_2Te_3/polyimide with ionic liquid	Screen printing	8 μW cm^{-2}	46	[149]
n-type: Bi_2Te_3 p-type: Sb_2Te_3	Screen printing	3800 μW cm^{-2}	50	[150]
p-type: PEDOT nanowires n-type: TiS_2: Hexylamine	Screen printing	47.8 μW cm^{-2}	30	[151]

the difficulties. Some of the widely used dopants like Te, though they helps to improve TE properties, are very harmful to the environment. Finding alternatives like p-type MgAgSb and n-type $Mg_3(Sb,Bi)_2$,[167] could be developed for the mass production of the TEDs. The field of printed thermoelectrics is relatively new, and a lot be explored in the coming years considering scopes for TED in a wide range of applications.

8. Conclusions

A paradigm shift from conventional bulk to printed thermoelectrics has been prominently observed in recent years to make the TE technology viable and cost effective. In addition, bulk thermoelectrics does not offer shape conformity, which is found to be essential in many applications on nonflat surfaces. The printed thermoelectrics could enable the low-cost production of shape-conformable TEDs. Initially, organic polymers have been targeted to make them high-performance printable TE materials. However, despite having good printability, their low TE performance limits their applications. This review reports the recent advances in inorganic-based printed thermoelectrics. Printable inorganic materials offer a pathway for overcoming these limitations. We have summarized the theoretical concepts of

thermoelectrics, the general TE ink formulation, the recent advancement of the inorganic and hybrid printed TE materials, and finally recently reported printed TEDs. It is obvious that the majority of the research on printed thermoelectrics has been carried out on inorganic $(BiSb)_2(TeSe)_3$-based TE materials. Nevertheless, other chalcogenides such as Ag_2Se and Cu_2Se have also shown promising performances. In addition, we have discussed the enhancement of the TE performance by hybridizing the inorganic TE materials with organic compounds. A figure-of-merit ZT ≈1 is achieved in printed $(BiSb)_2(TeSe)_3$-based TE materials. The printed TEG is reported to show a high-power output density as high as 1.88×10^4 μW cm^{-2}. These results pave the way to the manufacture of low-cost shape-conformable TEDs for waste heat recovery and energy harvesting applications.

Acknowledgements

Conflict of Interest

The authors declare no conflict of interest.

Keywords

chalcogenides, energy harvesting, printed thermoelectrics, tellurides, thermoelectric Generators

[1] Fitriani, R. Ovik, B. D. Long, M. C. Barma, M. Riaz, M. F. M. Sabri, S. M. Said, R. Saidur, *Renewable Sustainable Energy Rev.* **2016**, *64*, 635.

[2] B. Orr, A. Akbarzadeh, M. Mochizuki, R. Singh, *Appl. Therm. Eng.* **2016**, *101* 490.

[3] S. Nag, A. Dhar, A. Gupta, *Energy, Environment, and Sustainability*, Springer Publication, New York City, United States **2018**, https://doi.org/10.1007/978-981-16-8618-4.

[4] R. Rodriguez, M. Preindl, J. S. Cotton, A. Emadi, *IEEE Trans. Veh. Technol.* **2019**, *68*, 5366.

[5] D. M. Rowe, *CRC Handbook of Thermoelectrics*, CRC press, Florida, United States **1995**.

[6] N. LeMoyne, R. Mastroianni, T. Whiting, D. Tomycz, *Wearable and Wireless Systems For Healthcare II*, Springer Publication, New York City, United States **2019**.

[7] H. Cheng, Y. Du, B. Wang, Z. Mao, H. Xu, L. Zhang, Y. Zhong, W. Jiang, L. Wang, X. Sui, *Chem. Eng. J.* **2018**, *338*, 1.

[8] Mahanti, *Chemistry, Physics, and Materials Science Of Thermoelectric Materials: Beyond Bismuth Telluride*, Vol. 3, (Eds: M. G. Kanatzidis, T. P. Hogan), Springer, New York **2003**.

[9] J. Zang, J. Chen, Z. Chen, Y. Li, J. Zhang, T. Song, B. Sun, *J. Mater. Chem. A* **2021**, *9*, 19439.

[10] Z. Ouyang, D. Li, *Sci. Rep.* **2016**, *6*, 24123.

[11] D. M. Rowe, *Thermoelectrics Handbook: Macro to Nano*, CRC Press, Boca Raton, FL **2005**.

[12] G. Tan, L. D. Zhao, M. G. Kanatzidis, *Chem. Rev.* **2016**, *116*, 12123.

[13] C. Gayner, K. K. Kar, *Prog. Mater. Sci.* **2016**, *83*, 330.

[14] M. S. Hossain, T. Li, Y. Yu, J. Yong, J. H. Bahk, E. Skafidas, *RSC Adv.* **2020**, *10*, 8421.

[15] M. Orrill, S. LeBlanc, *J. Appl. Polym. Sci.* **2017**, *134*, 44256.

[16] B. Chen, S. R. Das, W. Zheng, B. Zhu, B. Xu, S. Hong, C. Sun, X. Wang, Y. Wu, J. C. Claussen, *Adv. Electron. Mater.* **2017**, *3*, 1600524.

[17] A. Sajedi-Moghaddam, E. Rahmanian, N. Naseri, *ACS Appl. Mater. Interfaces* **2020**, *12*, 34487.

[18] B. Chen, M. Kruse, B. Xu, R. Tutika, W. Zheng, M. D. Bartlett, Y. Wu, J. C. Claussen, *Nanoscale* **2018**, *11*, 5222.

[19] A. Besganz, V. Zöllmer, R. Kun, E. Pál, L. Walder, M. Busse, *Procedia Technol.* **2014**, *15*, 99.

[20] F. Jiao, C. A. Di, Y. Sun, P. Sheng, W. Xu, D. Zhu, *Philos. Trans. R. Soc., A* **2013**, *372*, 20130008.

[21] K. T. Park, J. Choi, B. Lee, Y. Ko, K. Jo, Y. M. Lee, J. A. Lim, C. R. Park, H. Kim, *J. Mater. Chem. A* **2018**, *6*, 19727.

[22] S. Ferhat, C. Domain, J. Vidal, D. Noël, B. Ratier, B. Lucas, *Sustainable Energy Fuels* **2017**, *2*, 199.

[23] O. Bubnova, Z. U. Khan, A. Malti, S. Braun, M. Fahlman, M. Berggren, X. Crispin, *Nat. Mater.* **2011**, *10*, 429.

[24] S. Y. Kim, K. Kim, Y. H. Hwang, J. Park, J. Jang, Y. Nam, Y. Kang, M. Kim, H. J. Park, Z. Lee, J. Choi, Y. Kim, S. Jeong, B. S. Bae, J. U. Park, *Nanoscale* **2016**, *8*, 17113.

[25] K. Kim, G. Kim, B. R. Lee, S. Ji, S. Y. Kim, B. W. An, M. H. Song, J. U. Park, *Nanoscale* **2015**, *7*, 13410.

[26] B. H. Kim, M. S. Onses, J. Bin Lim, S. Nam, N. Oh, H. Kim, K. J. Yu, J. W. Lee, J. H. Kim, S. K. Kang, C. H. Lee, J. Lee, J. H. Shin, N. H. Kim, C. Leal, M. Shim, J. A. Rogers, *Nano Lett.* **2015**, *15*, 969.

[27] J. Yong, Y. Liang, Y. Yu, B. Hassan, M. S. Hossain, K. Ganesan, R. R. Unnithan, R. Evans, G. Egan, G. Chana, E. Skafidas, *ACS Appl. Mater. Interfaces* **2019**, *11*, 17521.

[28] T. Varghese, C. Hollar, J. Richardson, N. Kempf, C. Han, P. Gamarachchi, D. Estrada, R. J. Mehta, Y. Zhang, *Sci. Rep.* **2016**, *6*, 33135.

[29] C. Navone, M. Soulier, M. Plissonnier, A. L. Seiler, *J. Electron. Mater.* **2010**, *39*, 1755.

[30] J. H. We, S. J. Kim, G. S. Kim, B. J. Cho, *J. Alloys Compd.* **2013**, *552*, 107.

[31] Z. Cao, E. Koukharenko, M. J. Tudor, R. N. Torah, S. P. Beeby, *Sens. Actuators, A* **2016**, *238*, 196.

[32] H. B. Lee, H. J. Yang, J. H. We, K. Kim, K. C. Choi, B. J. Cho, *J. Electron. Mater.* **2011**, *40*, 615.

[33] Q. Wei, M. Mukaida, K. Kirihara, Y. Naitoh, T. Ishida, *RSC Adv.* **2014**, *4*, 28802.

[34] K. Suemori, S. Hoshino, T. Kamata, *Appl. Phys. Lett.* **2013**, *103*, 153902.

[35] R. Rudež, P. Markowski, M. Presečnik, M. Košir, A. Dziedzic, S. Bernik, *Ceram. Int.* **2015**, *41*, 13201.

[36] A. Mahajan, C. D. Frisbie, L. F. Francis, *ACS Appl. Mater. Interfaces* **2013**, *5*, 4856.

[37] E. Jin Bae, Y. Hun Kang, K. S. Jang, S. Yun Cho, *Sci. Rep.* **2016**, *6*, 18805.

[38] C. T. Hong, Y. H. Kang, J. Ryu, S. Y. Cho, K. S. Jang, *J. Mater. Chem. A* **2015**, *3*, 21428.

[39] C. Ou, A. L. Sangle, T. Chalklen, Q. Jing, V. Narayan, S. Kar-Narayan, *APL Mater.* **2018**, *6*, 096101.

[40] A. Chen, D. Madan, P. K. Wright, J. W. Evans, *J. Micromech. Microeng.* **2011**, *21*, 104006.

[41] D. Madan, Z. Wang, A. Chen, R. Winslow, P. K. Wright, J. W. Evans, *Appl. Phys. Lett.* **2013**, *104*, 013902.

[42] D. Madan, Z. Wang, P. K. Wright, J. W. Evans, *Appl. Energy* **2015**, *156*, 587.

[43] R. R. Søndergaard, M. Hösel, N. Espinosa, M. Jørgensen, F. C. Krebs, *Energy Sci. Eng.* **2013**, *1*, 81.

[44] S. H. Ahn, L. J. Guo, *Adv. Mater.* **2008**, *20*, 2044.

[45] S. Dilfer, R. C. Hoffmann, E. Dörsam, *Appl. Surf. Sci.* **2014**, *320*, 634.

[46] A. Sandstrom, H. F. Dam, F. C. Krebs, L. Edman, *Nat. Commun.* **2012**, *3*, 1002.

[47] C. Amruth, D. K. Dubey, M. Pahlevani, G. C. Welch, *Adv. Mater. Technol.* **2021**, *6*, 2100264.

[48] F. C. Krebs, *Sol. Energy Mater. Sol. Cells* **2009**, *93*, 1636.

[49] J. E. Kim, S. S. Kim, C. Zuo, M. Gao, D. Vak, D. Y. Kim, *Adv. Funct. Mater.* **2019**, *29*, 1809194.

[50] S. Song, K. T. Lee, C. W. Koh, H. Shin, M. Gao, H. Y. Woo, D. Vak, J. Y. Kim, *Energy Environ. Sci.* **2018**, *11*, 3248.

[51] G. H. Kim, L. Shao, K. Zhang, K. P. Pipe, *Nat. Mater.* **2013**, *12*, 719.

[52] Y. Sun, P. Sheng, C. Di, F. Jiao, W. Xu, D. Qiu, D. Zhu, *Adv. Mater.* **2012**, *24*, 932.

[53] Q. Jiang, J. Yang, P. Hing, H. Ye, *Mater. Adv.* **2020**, *1*, 1038.

**ADVANCED
SCIENCE NEWS**

www.advancedsciencenews.com

**ADVANCED
ENGINEERING
MATERIALS**

www.aem-journal.com

[54] E. Jang, P. Banerjee, J. Huang, D. Madan, *Appl. Energy* **2021**, *294*, 117006.

[55] M. M. Mallick, A. Sarbajna, A. G. Rösch, L. Franke, H. Geßwein, Y. M. Eggeler, U. Lemmer, *Appl. Mater. Today* **2022**, *26*, 101269.

[56] Z. Cao, E. Koukharenko, M. J. Tudor, R. N. Torah, S. P. Beeby, *J. Phys. Conf. Ser.* **2013**, *476*, 012016.

[57] C. Wood, *Rep. Prog. Phys.* **1988**, *51*, 459.

[58] T. J. Seebeck, *Ann. Phys.* **1826**, *82*, 1.

[59] C. Goupil, *Continuum Theory and Modeling of Thermoelectric Elements*, 1st ed., Wiley-VCH Verlag GmbH & Co. KGaA, New Jersey, United States **2016**.

[60] J. M. Ziman, *Electrons and Phonons: The Theory of Transport Phenomena in Solids*, Oxford University Press, Oxford, UK **2001**.

[61] V. I. Fistul, *Heavily Doped Semiconductors*, Vol. *1*, Springer Publication, New York City, United States **2012**.

[62] N. F. Mott, E. A. Davis, *Electronic Processes in Non-Crystalline Materials*, Oxford University Press, Oxford, UK **2012**.

[63] S. Dongmin Kang, G. Jeffrey Snyder, *Nat. Mater.* **2016**, *16*, 252.

[64] G. S. Nolas, J. Sharp, J. Goldsmid, *Thermoelectrics: Basic Principles and New Materials Developments*, Vol. *45*, Springer Publication, New York City, United States **2010**.

[65] K. Yazawa, A. Shakouri, *J. Appl. Phys.* **2012**, *111*, 024509.

[66] C. Goupil, *Continuum Theory and Modeling of Thermoelectric Elements*, Wiley-VCH, New Jersey, United States **2016**.

[67] S. Il Kim, K. H. Lee, H. A. Mun, H. S. Kim, S. W. Hwang, J. W. Roh, D. J. Yang, W. H. Shin, X. S. Li, Y. H. Lee, G. J. Snyder, S. W. Kim, *Science* **2015**, *348*, 109.

[68] J. Feng, W. Zhu, Y. Deng, Q. Song, Q. Zhang, *ACS Appl. Energy Mater.* **2018**, *1*, 5646.

[69] A. L. Pires, I. F. Cruz, J. Silva, G. N. P. Oliveira, S. Ferreira-Teixeira, A. M. L. Lopes, J. P. Araújo, J. Fonseca, C. Pereira, A. M. Pereira, *ACS Appl. Mater. Interfaces* **2019**, *11*, 8969.

[70] C. Hollar, Z. Lin, M. Kongara, T. Varghese, C. Karthik, J. Schimpf, J. Eixenberger, P. H. Davis, Y. Wu, X. Duan, Y. Zhang, D. Estrada, *Adv. Mater. Technol.* **2020**, *5*, 2000600.

[71] Z. Lu, M. Layani, X. Zhao, L. P. Tan, T. Sun, S. Fan, Q. Yan, S. Magdassi, H. H. Hng, *Small* **2014**, *10*, 3551.

[72] Y. Du, J. Chen, X. Liu, C. Lu, J. Xu, B. Paul, P. Eklund, *Coatings* **2018**, *8*, 25.

[73] D. Madan, A. Chen, P. K. Wright, J. W. Evans, *J. Appl. Phys.* **2011**, *109*, 034904.

[74] J. Weber, K. Potje-Kamloth, F. Haase, P. Detemple, F. Völklein, T. Doll, *Sens. Actuators, A* **2006**, *132*, 325.

[75] L. D. Zhao, B. P. Zhang, J. F. Li, M. Zhou, W. S. Liu, *Physica B* **2007**, *400*, 11.

[76] D. Madan, Z. Wang, A. Chen, R. C. Juang, J. Keist, P. K. Wright, J. W. Evans, *ACS Appl. Mater. Interfaces* **2012**, *4*, 6117.

[77] M. J. Smith, R. J. Knight, C. W. Spencer, *J. Appl. Phys.* **2004**, *33*, 2186.

[78] H. J. Goldsmid, R. W. Douglas, *Br. J. Appl. Phys.* **1954**, *5*, 386.

[79] C. W. Nan, *Prog. Mater. Sci.* **1993**, *37*, 1.

[80] I. Webman, J. Jortner, M. H. Cohen, *Phys. Rev. B* **1977**, *16*, 2959.

[81] L. D. Zhao, B. P. Zhang, W. S. Liu, H. L. Zhang, J. F. Li, *J. Alloys Compd.* **2009**, *467*, 91.

[82] A. G. Rösch, F. Giunta, M. M. Mallick, L. Franke, A. Gall, J. Aghassi-Hagmann, J. Schmalian, U. Lemmer, *Adv. Theor. Simul.* **2021**, *4*, 2000284.

[83] D. B. Hyun, J. S. Hwang, B. C. You, T. S. Oh, C. W. Hwang, *J. Mater. Sci.* **1998**, *33*, 5595.

[84] G. R. Miller, C. Y. Li, *J. Phys. Chem. Solids* **1965**, *26*, 173.

[85] Z. Starý, J. Horák, M. Stordeur, M. Stölzer, *J. Phys. Chem. Solids* **1988**, *49*, 29.

[86] D. Madan, Z. Wang, A. Chen, P. K. Wright, J. W. Evans, *ACS Appl. Mater. Interfaces* **2013**, *5*, 11872.

[87] D. M. Rowe, *CRC Handbook of Thermoelectrics*, CRC press, Florida, United States **2010**.

[88] B. Poudel, Q. Hao, Y. Ma, Y. Lan, A. Minnich, B. Yu, X. Yan, D. Wang, A. Muto, D. Vashaee, X. Chen, J. Liu, M. S. Dresselhaus, G. Chen, Z. Ren, *Science* **2008**, *320*, 634.

[89] D. Madan, A. Chen, P. K. Wright, J. W. Evans, *J. Electron. Mater.* **2012**, *41*, 1481.

[90] J. P. Fleurial, L. Gailliard, R. Triboulet, H. Scherrer, S. Scherrer, *J. Phys. Chem. Solids* **1988**, *49*, 1237.

[91] L. M. Goncalves, C. Couto, P. Alpuim, A. G. Rolo, F. Völklein, J. H. Correia, *Thin Solid Films* **2010**, *518*, 2816.

[92] Y. Zhang, R. J. Mehta, M. Belley, L. Han, G. Ramanath, T. Borca-Tasciuc, *Appl. Phys. Lett.* **2012**, *100*, 193113.

[93] S. Shin, R. Kumar, J. W. Roh, D. S. Ko, H. S. Kim, S. Il Kim, L. Yin, S. M. Schlossberg, S. Cui, J. M. You, S. Kwon, J. Zheng, J. Wang, R. Chen, *Sci. Rep.* **2017**, *7*, 7317.

[94] S. A. Bahmani, G. C. East, I. Holme, *J. Soc. Dye. Colour.* **2006**, *116*, 94.

[95] H. Wang, T. Guo, H. Li, *J. Appl. Polym. Sci.* **2016**, *133*, 43997.

[96] P. S. R. Choi, C. W. M. Yuen, S. K. A. Ku, C. W. Kan, *Fibers Polym.* **2005**, *6*, 229.

[97] S. Noppakundilograt, P. Buranagul, W. Graisuwan, C. Koopipat, S. Kiatkamjornwong, *Carbohydr. Polym.* **2010**, *82*, 1124.

[98] Y. Zhu, *Int. J. Heat Mass Transf.* **2016**, *92*, 784.

[99] E. Dechaumphai, J. L. Barton, J. R. Tesmer, J. Moon, Y. Wang, G. R. Tynan, R. P. Doerner, R. Chen, *J. Nucl. Mater.* **2014**, *455*, 56.

[100] E. Dechaumphai, D. Lu, J. J. Kan, J. Moon, E. E. Fullerton, Z. Liu, R. Chen, *Nano Lett.* **2014**, *14*, 2448.

[101] B. Xu, M. T. Agne, T. Feng, T. C. Chasapis, X. Ruan, Y. Zhou, H. Zheng, J. H. Bahk, M. G. Kanatzidis, G. J. Snyder, Y. Wu, *Adv. Mater.* **2017**, *29* https://doi.org/, 1605140.

[102] H. Fang, T. Feng, H. Yang, X. Ruan, Y. Wu, *Nano Lett.* **2013**, *13*, 2058.

[103] H. Yang, J. H. Bahk, T. Day, A. M. S. Mohammed, G. J. Snyder, A. Shakouri, Y. Wu, *Nano Lett.* **2015**, *15*, 1349.

[104] R. Danaei, T. Varghese, M. Ahmadzadeh, J. McCloy, C. Hollar, M. Sadeq Saleh, J. Park, Y. Zhang, R. Panat, *Adv. Eng. Mater.* **2019**, *21*, 1800800.

[105] W. MacNeill, C. H. Choi, C. H. Chang and R. Malhotra, *Sci. Rep.* **2015**, *5*, 14845.

[106] S. Bansal, R. Malhotra, *Nanotechnology* **2016**, *27*, 495602.

[107] M. Saeidi-Javash, W. Kuang, C. Dun, Y. Zhang, *Adv. Funct. Mater.* **2019**, *29*, 1901930.

[108] T. Varghese, C. Dun, N. Kempf, M. Saeidi-Javash, C. Karthik, J. Richardson, C. Hollar, D. Estrada, Y. Zhang, *Adv. Funct. Mater.* **2019**, *30* https://doi.org/, 1905796.

[109] J. S. Son, H. Zhang, J. Jang, B. Poudel, A. Waring, L. Nally, D. V. Talapin, *Angew. Chem., Int. Ed.* **2014**, *53*, 7466.

[110] L. Wang, Z. Zhang, Y. Liu, B. Wang, L. Fang, J. Qiu, K. Zhang, S. Wang, *Nat. Commun.* **2018**, *9*, 3817.

[111] X. Mu, H. Zhou, D. He, W. Zhao, P. Wei, W. Zhu, X. Nie, H. Liu, Q. Zhang, *Nano Energy* **2017**, *33*, 55.

[112] J. Feng, W. Zhu, Z. Zhang, L. Cao, Y. Yu, Y. Deng, *ACS Appl. Mater. Interfaces* **2020**, *12*, 16630.

[113] H. Choi, S. J. Kim, Y. Kim, J. H. We, M. W. Oh, B. J. Cho, *J. Mater. Chem. C* **2017**, *5*, 8559.

[114] Y. Zhang, L. P. Hu, T. J. Zhu, J. Xie, X. B. Zhao, *Cryst. Growth Des.* **2013**, *13*, 645.

[115] M. M. Rashad, A. El-Dissouky, H. M. Soliman, A. M. Elseman, H. M. Refaat, A. Ebrahim, *Mater. Res. Innov.* **2017**, *22*, 315.

[116] Y. Liu, V. Khavrus, T. Lehmann, H. L. Yang, L. Stepien, M. Greifzu, S. Oswald, T. Gemming, V. Bezugly, G. Cuniberti, *ACS Appl. Energy Mater.* **2020**, *3*, 2556.

[117] W. Zeng, X. M. Tao, S. Lin, C. Lee, D. Shi, K. Ho Lam, B. Huang, Q. Wang, Y. Zhao, *Nano Energy* **2018**, *54*, 163.

[118] J. Choi, Y. Jung, S. J. Yang, J. Y. Oh, J. Oh, K. Jo, J. G. Son, S. E. Moon, C. R. Park, H. Kim, *ACS Nano* **2017**, *11*, 7608.

[119] J. L. Blackburn, A. J. Ferguson, C. Cho, J. C. Grunlan, *Adv. Mater.* **2018**, *30*, 1704386.

[120] D. Ding, F. Sun, F. Xia, Z. Tang, *Nanoscale Adv.* **2020**, *2*, 3244.

[121] X. Li, J. Yin, J. Zhou, Q. Wang, W. Guo, *Appl. Phys. Lett.* **2012**, *100*, 183108.

[122] Y. Zhao, G. S. Tang, Z. Z. Yu, J. S. Qi, *Carbon* **2012**, *55*, 3885.

[123] R. Pasricha, S. Gupta, A. K. Srivastava, *Small* **2009**, *5*, 2253.

[124] M. M. Mallick, A. G. Rösch, L. Franke, S. Ahmed, A. Gall, H. Geßwein, J. Aghassi, U. Lemmer, *ACS Appl. Mater. Interfaces*, **2020**, *12*, 19655.

[125] H. Z. Duan, Y. L. Li, K. P. Zhao, P. F. Qiu, X. Shi, L. D. Chen, *JOM* **2016**, *68*, 2659.

[126] M. M. Mallick, A. G. Rösch, L. Franke, A. Gall, S. Ahmad, H. Geßwein, A. Mazilkin, C. Kübel, U. Lemmer, *J. Mater. Chem. A* **2020**, *8*, 16366.

[127] M. Mofasser Mallick, L. Franke, A. G. Rösch, S. Ahmad, H. Geßwein, Y. M. Eggeler, M. Rohde, U. Lemmer, *ACS Appl. Mater. Interfaces* **2021**, *13*, 61386.

[128] X. Shi, H. Chen, F. Hao, R. Liu, T. Wang, P. Qiu, U. Burkhardt, Y. Grin, L. Chen, *Nat. Mater.* **2018**, *17*, 421.

[129] Z. Gao, Q. Yang, P. Qiu, T. R. Wei, S. Yang, J. Xiao, L. Chen, X. Shi, *Adv. Energy Mater.* **2021**, *11*, 2100883.

[130] J. Liang, T. Wang, P. Qiu, S. Yang, C. Ming, H. Chen, Q. Song, K. Zhao, T. R. Wei, D. Ren, Y. Y. Sun, X. Shi, J. He, L. Chen, *Energy Environ. Sci.* **2019**, *12*, 2983.

[131] S. Yang, Z. Gao, P. Qiu, J. Liang, T. R. Wei, T. Deng, J. Xiao, X. Shi, L. Chen, *Adv. Mater.* **2021**, *33*, 2007681.

[132] J. H. We, S. J. Kim, B. J. Cho, *Energy* **2014**, *73*, 506.

[133] X. Zhao, D. Madan, Y. Cheng, J. Zhou, H. Li, S. M. Thon, A. E. Bragg, M. E. DeCoster, P. E. Hopkins, H. E. Katz, *Adv. Mater.* **2017**, *29*, 1606928.

[134] D. Yoo, J. J. Lee, C. Park, H. H. Choi, J. H. Kim, *RSC Adv.* **2016**, *6*, 37130.

[135] Y. Chen, M. He, B. Liu, G. C. Bazan, J. Zhou, Z. Liang, *Adv. Mater.* **2016**, *29*, 1604752.

[136] Y. Chen, Y. Zhao, Z. Liang, *Energy Environ. Sci.* **2014**, *8*, 401.

[137] A. Datta, A. Sangle, N. Hardingham, C. Cooper, M. Kraan, D. Ritchie, V. Narayan, S. Kar-Narayan, *Materials* **2017**, *10*, 553.

[138] M. S. Dresselhaus, G. Chen, M. Y. Tang, R. Yang, H. Lee, D. Wang, Z. Ren, J. P. Fleurial, P. Gogna, *Adv. Mater.* **2007**, *19*, 1043.

[139] A. Datta, J. Paul, A. Kar, A. Patra, Z. Sun, L. Chen, J. Martin, G. S. Nolas, *Cryst. Growth Des.* **2010**, *10*, 3983.

[140] B. Zhang, J. Sun, H. E. Katz, F. Fang, R. L. Opila, *ACS Appl. Mater. Interfaces* **2010**, *2*, 3170.

[141] O. Bubnova, Z. U. Khan, H. Wang, S. Braun, D. R. Evans, M. Fabretto, P. Hojati-Talemi, D. Dagnelund, J. B. Arlin, Y. H. Geerts, S. Desbief, D. W. Breiby, J. W. Andreasen, R. Lazzaroni, W. M. Chen, I. Zozoulenko, M. Fahlman, P. J. Murphy, M. Berggren, X. Crispin, *Nat. Mater.* **2014**, *13*, 190.

[142] C. Ou, A. L. Sangle, A. Datta, Q. Jing, T. Busolo, T. Chalklen, V. Narayan, S. Kar-Narayan, *ACS Appl. Mater. Interfaces* **2018**, *10*, 19580.

[143] J. H. Bahk, H. Fang, K. Yazawa, A. Shakouri, *J. Mater. Chem. C* **2015**, *3*, 10362.

[144] Y. Du, K. F. Cai, S. Chen, P. Cizek, T. Lin, *ACS Appl. Mater. Interfaces* **2014**, *6*, 5735.

[145] S. K. Yee, N. E. Coates, A. Majumdar, J. J. Urban, R. A. Segalman, *Phys. Chem. Chem. Phys.* **2013**, *15*, 4024.

[146] Y. Du, J. Chen, Q. Meng, J. Xu, J. Lu, B. Paul, P. Eklund, *Adv. Electron. Mater.* **2020**, *6*, 2000214.

[147] Z. Z. Zhang, G. Q. Lu, *IEEE Trans. Electron. Packag. Manuf.* **2002**, *25*, 279.

[148] Y. Du, J. Chen, Q. Meng, J. Xu, B. Paul, P. Eklund, *J. Mater.* **2020**, *6*, 293.

[149] K. Kato, K. Kuriyama, T. Yabuki, K. Miyazaki, *J. Phys. Conf. Ser.* **2018**, *1052*, 012008.

[150] S. J. Kim, J. H. We, B. J. Cho, *Energy Environ. Sci.* **2014**, *7*, 1959.

[151] A. G. Rösch, A. Gall, S. Aslan, M. Hecht, L. Franke, M. M. Mallick, L. Penth, D. Bahro, D. Friderich, U. Lemmer, *npj Flexible Electron.* **2021**, *5*, 1.

[152] W. Hou, X. Nie, W. Zhao, H. Zhou, X. Mu, W. Zhu, Q. Zhang, *Nano Energy* **2018**, *50*, 766.

[153] M. Zeng, Y. Zhang, *J. Mater. Chem. A* **2019**, *7*, 2330.

[154] G. Hu, J. Kang, L. W. T. Ng, X. Zhu, R. C. T. Howe, C. G. Jones, M. C. Hersam, T. Hasan, *Chem. Soc. Rev.* **2018**, *47*, 3265.

[155] B. Xu, T. Feng, Z. Li, W. Zheng, Y. Wu, *Adv. Mater.* **2018**, *30*, 1801904.

[156] M. M. Mallick, L. Franke, A. G. Rösch, H. Geßwein, Y. M. Eggeler, U. Lemme, *ACS Omega* **2022**, *7*, 10695.

[157] F. Kim, B. Kwon, Y. Eom, J. E. Lee, S. Park, S. Jo, S. H. Park, B. S. Kim, H. J. Im, M. H. Lee, T. S. Min, K. T. Kim, H. G. Chae, W. P. King, J. S. Son, *Nat. Energy* **2018**, *3*, 301.

[158] R. J. Mehta, Y. Zhang, C. Karthik, B. Singh, R. W. Siegel, T. Borca-Tasciuc, G. Ramanath, *Nat. Mater.* **2012**, *11*, 233.

[159] Z. Wang, W. Cui, H. Yuan, X. Kang, Z. Zheng, L. Chen, Q. Hu, W. Qiu, J. Tang, X. Cui, *JMCA* **2022**, *10*, 12921.

[160] R. Nayaka, P. Shetty, M. Selvakumar, A. Rao, K. M. Rao, K. Gurukrishna, S. Mangavati, *J. Alloys Compd.* **2022**, *922*, 166298.

[161] S. Chien, L. Hou, C. Li, C. Liao, *Mater. Chem. Phys.* **2022**, *287*, 126269.

[162] X. Tao, B. W. Stuart, H. E. Assender, *Surf. Coat. Technol.* **2022**, *447*, 128826.

[163] K. Suemori, T. Nobeshima, S. Uemura, N. Fukuda, *Adv. Mater. Technol.* **2022**, *7*, 202100473.

[164] J. Xie, M. Han, X. Zeng, D. Mao, H. Li, X. Zeng, R. Liu, L. Ren, R. Sun, J. Xu, *Chem. Eng. J.* **2022**, *435*, 135172.

[165] A. Amin, R. Huang, D. Newbrook, V. Sethi, S. Yong, S. Beeby, I. Nandhakumar, *IOP J. Phys. Energy* **2022**, *4*, 024003.

[166] M. M. Mallick, L. Franke, A. G. Rösch, H. Geßwein, Z. Long, Y. M. Eggeler, U. Lemme, *Adv. Sci.* **2022**, 2202411, https://doi.org/10.1002/advs.202202411.

[167] P. Ying, R. He, J. Mao, Q. Zhang, H. Reith, J. Sui, Z. Ren, K. Nielsch, G. Schierning, *Nat. Commun.* 1121, *12*, **2021**.

**ADVANCED
SCIENCE NEWS**

www.advancedsciencenews.com

**ADVANCED
ENGINEERING
MATERIALS**

www.aem-journal.com

Avishek Sarbajna is a doctoral research scholar in the department of physics at the Technical University of Denmark. He received his M.Sc. in Optics and Photonics from the School of Optics and Photonics, Karlsruhe Institute of Technology in 2021. His research interests include thermoelectric material, quantum light sources, two-dimensional materials, and nanofabrication.

Andres Rösch is an electrical engineer and Ph.D. candidate at KIT Karlsruhe, Germany. His Ph.D. thesis focuses on the design and simulation of printable thermoelectric materials and generators. His work is published in high impact journals and included simulation of novel printable composite thermoelectric materials and the design and fabrication of fully printed origami-folded devices for energy harvesting and waste heat recovery applications. His goal is to further the development of highly efficient low-cost market competitive thermoelectric devices to improve energy efficiency in industrial processes.

Leonard Franke is a mechanical engineer and Ph.D. student at the Karlsruhe Institute of Technology (KIT). His work focuses on printed thermoelectrics, in particular on the design, fabrication, and simulation of printed thermoelectric devices. With his work, he pursues the aim of developing more competitive printed thermoelectric devices for heat recovery, sensing, and cooling applications.

Uli Lemmer received the Diploma degree from RWTH Aachen University in 1990 and a Ph.D. from the University of Marburg in 1995. He then held a postdoctoral position with the University of California at Santa Barbara. Afterwards, he was heading the Organic Optoelectronics group at the University of Munich from 1996 to 2002. In 2002, he was appointed a full Professor of Electrical Engineering and Information Technology and Director of the Light Technology Institute, Karlsruhe Institute of Technology (KIT). His research interests are in the field of optoelectronics and the technology and the applications of printable organic and inorganic materials.

Mofasser Mallick is a postdoctoral researcher at Karlsruhe Institute of Technology. He received his M.Sc. from IIEST Shibpur. He completed his Master of Technology from IIT Kharagpur. He received his Ph.D. from IIT Bombay in 2018 and his doctoral thesis focused on the development of high-temperature thermoelectric materials. Based on his Ph.D. works, he was awarded the "Award of Excellence in Ph.D. Research." His research interest includes high-efficiency printed thermoelectric materials for large-scale applications and other printed functional materials.